STEP Enabled Polymeric Based Fibrous Scaffolds for the Study of Group Cell Migration and Cell Contractile Forces

Colin Uber Ng

Thesis submitted to the faculty of the Virginia Polytechnic Institute and State University in partial fulfillment of the requirements for the degree of

Master of Science

In

Mechanical Engineering

Amrinder S. Nain

Bahareh Behkam

Rakesh K. Kapania

December 10, 2013

Blacksburg, Virginia

nanofibers, group cell migration, cell forces, wound healing

STEP Enabled Polymeric Based Fibrous Scaffolds for the Study of Group Cell Migration and Cell Contractile Forces

Colin Uber Ng

ABSTRACT

Spinneret based Tunable Engineered Parameters (STEP) Platform is a recently reported pseudo-dry spinning and non-electrospinning technique that allows for the deposition of aligned polymeric nano-fibers with control on fiber diameters and orientation in single and multiple layers (diameter: sub 100nm –micron, length: mm-cm), deposition (parallelism ≤ 2.5 degrees) and spacing (microns)). A wide range of polymers such as PLGA, PLA, PS, and PU have been utilized for their unique material properties in scaffold design. In this thesis two unique bioscaffolds are demonstrated for the measurement of group cell migration for wound closure and single cell contractility force for the study of force modulation.

The wound healing assay bridges the gap between confluent reservoirs of NIH3T3 fibroblasts through arrangement of a suspended array of fibers guiding group cell migration along the fiber axis. This platform demonstrates that topographical and geometrical features of suspended fibers play a very important role in wound closure. Spacing, alignment and orientation were optimized to show an increased rate of closure. In the second complementary assay, we report a fused-fiber network of suspended fibers capable of measuring single cell forces. Results from our experiments demonstrate that force behavior is dependent on mechanical properties such as stiffness and geometry of fiber networks. We also demonstrate changes in spatial and temporal organization of focal adhesion zyxin in response to single cell migration on these networks.

Table of Contents

List of Figures

Chapter 1:

Nanofiber Manufacturing with STEP Technique

1.1 STEP Fiber Manufacturing

STEP (Spinneret based Tunable Engineered Parameters) is a psuedo-dry spinning technique capable of depositing highly aligned polymeric fibers with control on fiber dimensions (diameter: sub 100nm – micron, length: mm-cm), deposition (parallelism ≤ 2.5 degrees) and spacing (sub 100nm-microns) compared to current state-of-the-art fiber deposition techniques. In addition, a wide variety of polymeric systems have been utilized with this technique including PMMA, PLGA, PLA, PS, PU and PEO. With the ability to control fabrication parameters independently, fibrous biomedical scaffolds can be created with user-desired geometry, stiffness and size. The effects of modifying individual parameters on cellular response are explored through both our force platform and wound healing assay. [12]

STEP platform (Figure 1) works by drawing a polymeric solution out of a small capillary by the application of a mechanical pressure, forming a droplet at the tip. Upon contacting this droplet with a rotating substrate, the surface tension is broken and fibers are drawn onto the substrate. Solvent evaporates from the solution when drawn, leaving only a dry polymer deposited onto the final scaffold. The extruded droplet acts an infinite reservoir that enables constant fiber deposition. The rotating substrate is then translated allowing the deposition of layers. Further layers can be added at different orientations to complete the scaffold.

The uniqueness of this platform comes in the method in which the surface tension of the droplet is broken. In electrospinning, the current standard of fiber deposition, the application of large electric potential between the substrate and the capillary causes the fibers to be randomly ejected onto the substrate. In contrast, STEP utilizes a shearing force between the droplet and the rotating substrate to break the surface tension and draw out the fibers. This key difference enables STEP platform to have a higher control of the fiber deposition because it removes the inherent instability associated with high voltage potentials. [34]

1.2 Parameter Control

A wide variety of parameters are used to manipulate the fiber morphology such as solution rheology, rotational speed, substrate size, capillary diameter, atmospheric environment and flow rate. In addition, parameters such as substrate geometry, rotational speed, translational speed and substrate orientation are used to manipulate the fiber geometry of the scaffold. All of these factors are highlighted in Figure 1and will be further explained in detail with respect to its effect on fiber diameter, tension, spacing and hierarchal structures.

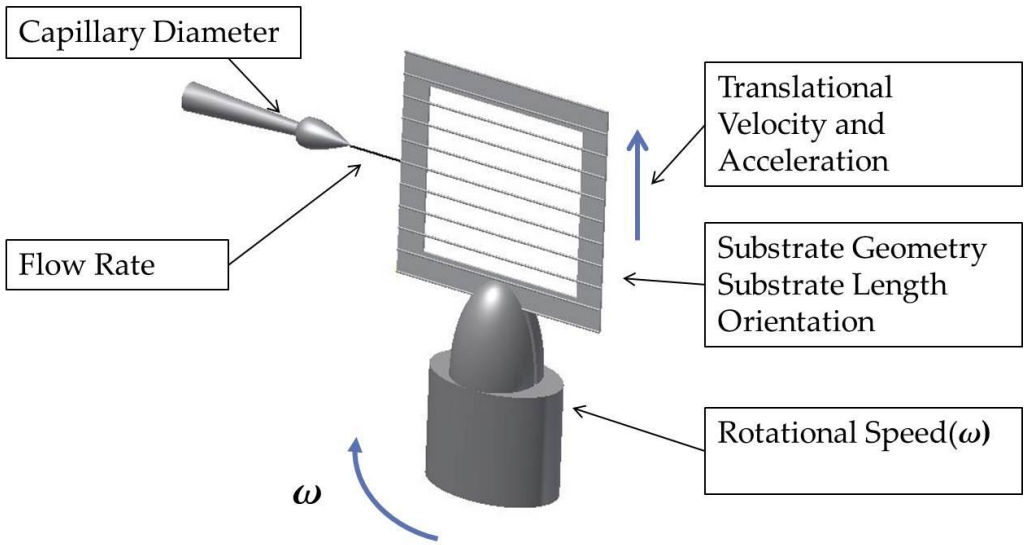

Figure 1 shows the parameter control in STEP platform. Capillary diameter, flow rate, translational velocity and acceleration, substrate dimensions and rotational speed allow for a high control of fiber deposition

1.3 Fiber Diameter

Fiber diameter is controlled by both the solution rheology and the flow parameters. We control the solution rheology by altering the solvent type and polymer concentration while still providing enough molecular chain entanglements to successfully draw the fibers. Increasing the polymer concentration will increase the fiber diameter but in the process will make the solution more viscous. If the solution becomes too viscous, the fiber cannot be drawn from the capillary. The same problem occurs when the solution is too dilute where the polymer chains are too far apart to entangle and form fibers. In addition, the choice of solvent also directly affects the fiber diameter. More volatile solvents with lower boiling points will create larger diameter fibers.

Another approach to altering the fiber diameter is changing the rotational rate of the substrate. Higher rotational speeds will draw the fiber faster and produce smaller diameter fibers. However, if the rotational rate becomes too high, the droplet cannot be replenished fast enough to maintain a continuous stream of polymer. Conversely, if the rotational rate is too low, the solvent does not immediately evaporate upon fiber deposition causing unaligned and non-uniform diameter fibers.

Finally, the flow rate and capillary diameter play a primary role in diameter control. Changing the diameter of the capillary dictates your maximum and minimum capable diameter. A steady increase in flow rate will increase the fiber diameter until too much solution is extruded to maintain a steady jet. If the flow rate is too small, the solution is pulled faster than the solution can be replenished, preventing continuous fiber deposition.

1.4 Fiber Tension

Fiber tension is present in all STEP produced fibers. This is a result of the polymer stretching process required for successful fiber deposition which causes an inherent pre-strain in the fibers. Experimentally, using atomic force microscope (AFM), the magnitude of the tension has been shown to be closely related to the diameter of the fiber in PU systems (Figure 1.2). Figure 1.2A shows the linear force verse deflection plot of a fiber deflected laterally by an AFM cantilever. The tension of the beam is then calculated by fitting the beam model (described in the modeling section at the end of the chapter) to the

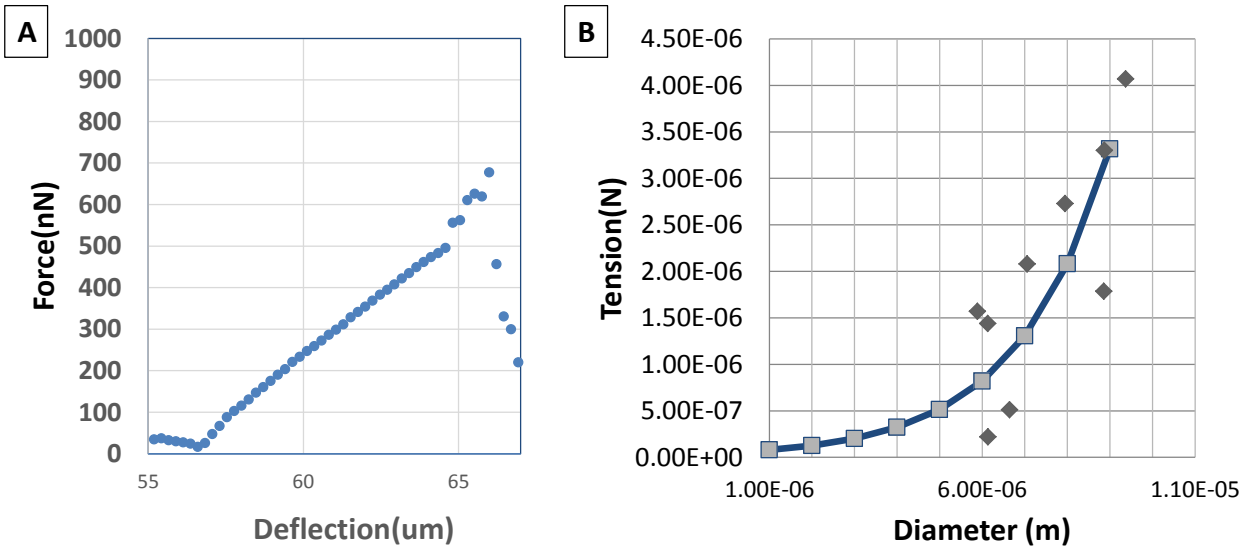

Figure 2 shows preliminary AFM data for our micro-beams. 2A shows a sample set of AFM data from which we calculated the tension in 2B. Initial results indicate the tension is related to the diameter of the fiber

AFM data and plotted in Figure 2B. This plot demonstrates that the tension is a function of diameter where the highest tension occurs with the largest diameter fibers.

Since the tension is a function of diameter, we use the fiber diameter as an indicator of the fiber tension. This simplifies the process by removing the need to measure the fiber stiffness of every scaffold.

1.5 Fiber Spacing

Spacing is controlled by varying the rotational rate and translational speed of the substrate. The relationship between the fiber spacing and the spinning parameters is as follows:

$$\boldsymbol{T = \omega * l} \qquad Equation\ 1$$

Where T is the constant translational speed in mm/second, $\boldsymbol{\omega}$ is the rotational speed in revolutions/second and $\boldsymbol{l}$ is the fiber spacing from center to center. This accurately represents fiber spacing as long as there is a stable jet and the desired spacing is greater than the diameter of the fibers.

Within the same scaffold, varied spacing can be achieved by accelerating the translational speed. The relationship is described as follows:

$$\boldsymbol{l = \sum_{n=1}^{nn} \left(\frac{a}{2\omega^3} (2n - 1) \right)} \qquad Equation\ 2$$

Where $\boldsymbol{l}$ is the matrix of fiber separations in ascending order, $\boldsymbol{nn}$ is the number of fibers deposited on one side, $\boldsymbol{a}$ is the acceleration in mm/second^2, $\boldsymbol{\omega}$ is the rotational speed in revolutions/second.

This expression is derived from incorporating an acceleration term in Equation 1 and relating it to the time required to deposit a single fiber (derived in Appendix B). This is also accurate at approximating the spacing in the same conditions as the constant velocity equation. However, the equation may deviate at high acceleration rates where it is difficult to maintain a constant jet.

1.6 Hierarchical Structures

Multilayered fiber scaffolds are easily achieved through substrate orientation, enabling the investigation of cell-fiber interactions such as cell shape and cytoskeletal organization. The most common

configuration is two layers laid perpendicular to each other and referred to as double suspended scaffold (3C). After spinning the first layer, the substrate is rotated 90 degrees and a second layer is spun over the top the previous layer. Fibers of different material properties and diameters can be spun within each layer allowing a high degree of customization in each scaffold. This same concept allows for angle

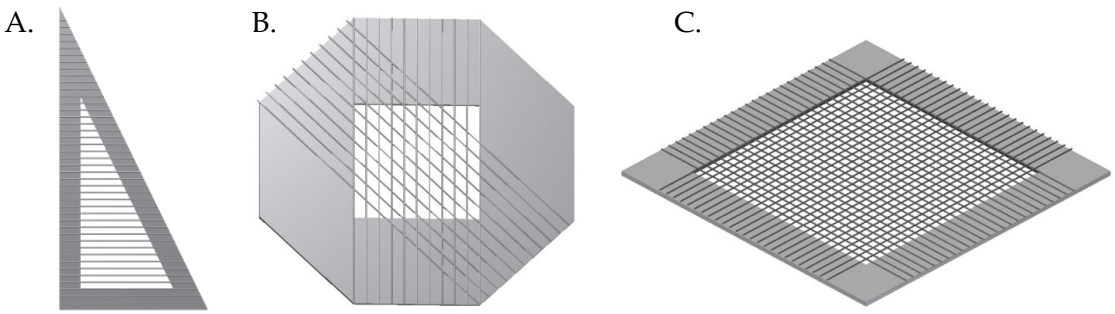

Figure 3 shows the range of substrate geometries. Angled fiber depositions are produced with right triangle (3A) or octagon substrates (3B). Orthogonal fiber arrays are deposited width rectangular substrates (3C).

control between multiple layers where diverging fiber arrays of a desired angle can be easily obtained. Substrate shape can be manipulated to improve angled fiber deposition by using a right triangular(3A) substrate with an acute angle of the desired fiber angle or octagon substrates(3B)

1.7 Fusing

Multilayered fiber structures can be fused together by exposing scaffolds to solvent vapor. The strength and speed of the fusing is dependent on vapor diffusion where an increase in the solvent flux increases the rate of scaffold fusion. Solvents with higher evaporation have a greater ability to fuse the scaffolds. This can be enhanced by heating the solvent thereby increasing the solvent vapor flux.

The effectiveness of the fusing process depends on the quality and the composition of the scaffold. Smaller diameter and sparsely dense fiber scaffolds require less flux to fuse compared to its denser larger diameter counterpart. Our method of fusion is described further in the next section.

1.8 Manufacturing Force Scaffolds

Designing and manufacturing force scaffolds is comprised of five steps that include:

1. Substrate Preparation
2. Base Layer Manufacturing (Support Layer)
3. Secondary Layer Manufacturing (Deforming Layer)
4. Layer Fusion
5. Validation, Coating and Imaging
6. Force Calculation

Each of these steps will be explained in detail in the following sections.

1.8.1 Substrate Preparation

Substrates are cut from plastic cover slips (0.2mm in thickness) into rectangular frames. Substrate dimensions do not directly affect the mechanical properties of the scaffold but will affect the spinnibility and alignment of the fibers. Very large scaffolds (>10mm) are more difficult to spin because of the substrate's greater unsteadiness during rotation and consists of more fragile higher aspect ratio fibers. In contrast very small substrates (<3mm) are more difficult to handle and have smaller working areas. As a result, the current standard is to use 6x6 mm frame substrates. These dimensions were chosen to maximize jet continuity in concurrence with maximizing substrate area. As a final note, the length of the

substrate will affect the edge velocity and must be considered when determining the rotational velocity later in the process.

1.8.2 Base Layer Manufacturing

The base layer provides the rigid boundary conditions required for the formation of deflectable micro-beams. Base layer fibers must remain rigid and stationary when exposed to either the cellular forces or the fusing vapors to maintain boundary conditions during force calculation. More specifically, the fusing process may cause the base layer to shift or fold the fibers, thus altering the scaffold geometry. In order to avoid this issue, the base layer diameters should be at least two to three times larger than the deformable layer. This allows for the successful fusing without destroying the force scaffold.

As long as these minimum concerns are met, the choice of base layer properties such as material diameter and spacing can be determined by the needs of the experiment. Currently, the standard base layer is composed of 5µm diameter polystyrene fibers spun from 10% (% w/w) polystyrene (M_w: 2Million) in 70 DMF : 30 Xylene(% v/v). `

Base layer spacing determines where and how the cell is pulling on the fiber. If the fiber spacing is too small, the cell interacts with both boundary conditions; if the spacing is too large, the cell only pulls on the edge of the beam, negating the fiber length. In both scenarios, the deflection of the fiber is typically no larger than two microns which is too small to effectively measure with our scope (a resolution of 0.43µm in 20x and 40x and a resolution of 0.24µm in 63x). Fiber spacing should be optimized to where the cell pulls at the center of the fiber where the deflection is largest. In order to achieve this, the scaffold parameters must be customized to the cell line. The current choice for NIH3T3 fibroblasts is a spacing of 130 µm created by a rotational rate of 40,000 µsteps/ second with a translation rate of 0.1 mm/s. At this spacing, the maximum number of fibroblasts causing the largest fiber deflections are observed.

In the case of contraction between two parallel fibers, a spacing of 200μm is chosen to ensure that cells can sufficiently migrate away from the boundaries. Larger fiber separations may be explored but it becomes more difficult to maintain a stable jet at the higher translational speeds and accelerations.

Some issues typically associated with base layer manufacturing comes with changes in the environmental humidity. Polystyrene tends to become statically charged in low humidity environments. As a result, the polystyrene fibers tend to stick together and lose their alignment. To prevent this issue, a high relative humidity is required to remove the static charges. Furthermore, if the base layer fibers are not in plane, the scaffold cannot be uniformly fused leaving unfused patches throughout the scaffold.

1.8.3 Deformable Layer Manufacturing

The cell force behavior is determined by the mechanical properties of the deformable layer. It is very important to control the fiber tension as it is the dominant component that determines the stiffness of each microbeam. If the tension is too large, the cells will be unable to deform the fibers. Conversely, if the tension is too low the fiber will produce nonlinear deflections voiding the Euler beam assumptions. Based off preliminary data the diameter of the fiber is a good indicator for the tension in the fibers and can be used as means to determine the tension in our fibers.

Choosing the ideal fiber characteristics is dependent on maximizing the fiber deflection while remaining under a strain of 10% required by Euler's assumptions. Both polystyrene and polyurethane have been shown to be successful in obtaining the necessary deflections. However, polyurethane is preferable because of its lower elastic modulus.

PU 26% Estane 5719 (Lubrizol) (w/w) in 70:30 DMF: THF (% v/v) solutions was chosen for its spinnability and fiber uniform surface morphology. The main issue of using this polymer solution is THF is a volatile solvent that has a low boiling point. As a result, the solution composition changes as the solvent

evaporates with each use. It necessary to make new polyurethane solutions after two uses or the fiber mechanical properties will not be repeatable between fiber depositions.

As mentioned above, determining the fiber stiffness is dependent on fiber diameter which is primarily controlled by rotational rate and capillary diameter size. The glass capillary is manufactured using a Flaving/Brown micropipette puller forming a sub-micron capillary tip diameter. The pipette is then further modified by cutting 5mm off the top of the capillary. The rotational rate is then varied between 30,000 µsteps/s to 150,000 µsteps/s to vary the fiber diameter to measure different forces. Scaffolds spun at 30,000 µsteps/s are suited for cells that exert larger forces such as C2C12s or Hepatocytes while 150,000 µsteps/s are suited for cells that exert smaller forces such as fibroblasts.

Spacing is varied on the same scaffold through using an accelerating translational speed. Standard parameters involve using 120,000 µsteps/s at an acceleration of 0.012mm/s^2 in 1mm bands. The acceleration should be adjusted accordingly with higher or lower rotational speeds to maintain the same spacing. These parameters will produce spacing between 5µm and 100µm allowing for the study of both single and double pull behavior in the same scaffold. As with the base layer, the deposited fibers must all be deposited in plane of one another or the fibers cannot be uniformly fused.

1.8.4 Fusing Layers

The fiber fusing process is demonstrated in Figure 4A. THF, a volatile solvent, is placed in a glass petri dish below a scaffold supported by parallel glass slides. As the solvent evaporates, the vapors diffuse through the scaffold fusing the fibers. The scaffolds are exposed to the solvent in intervals of 15 seconds (i.e. 15, 30, 45, 60, etc.) where the scaffold is flipped in between each interval. The number of intervals required to fuse the sample is dependent on the scaffold parameters. Scaffolds with denser fiber depositions (larger diameters and/or tighter spacings) require more sequential exposures than that of

scaffolds with small diameters and larger spacing. The rate of fusion may be enhanced by heating the underlying solvent. Images of the fused fibers are shown in Figure 4B and 4C.

1.8.5 Validation, Coating and Imaging

Fused-fiber scaffolds are placed in the 6 well plate and sterilized by immersing them in ethanol. After sterilization, the fibers need to be coated with an ECM protein in order to aid cell attachment. Fibers are typically coated with 2µg/mL fibronectin and placed in the incubator for at least 2 hours before cells are seeded on the scaffolds. The cells were allowed to attach for four hours prior to time-lapse imaging. Standard imaging is conducted over 6 hours using a Zeiss microscope with incubating capacity.

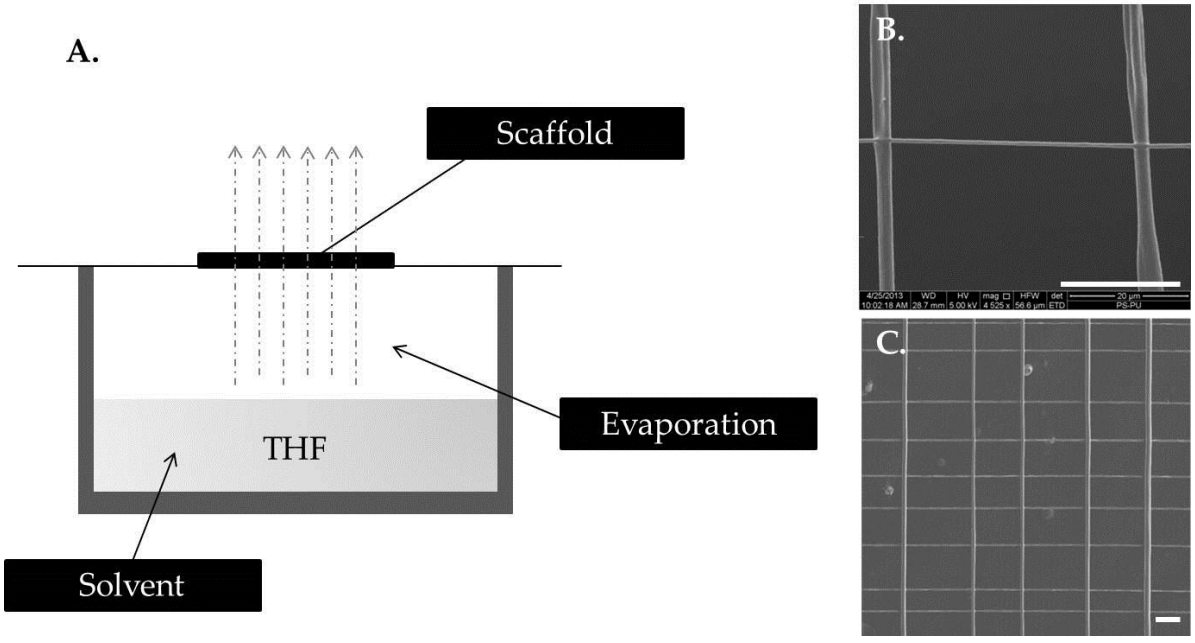

Figure 4 shows the fiber fusing process. 4A shows how the solvent vapors diffuse through the fiber scaffold, fusing the fibers. 4B and 4C show ESEM images of the fiber and layer fusion

1.8.6 Force Calculation Model

Forces were calculated by modeling the fiber as a beam with pin-roller boundary conditions under both axial and lateral loads. Figure 5 shows the load assumptions for, single cell-fiber interaction and single cell-double fiber interaction. In both cases, the cells are assumed to exert a non-uniform distributed load on the beam. The force vectors are determined from the cell phase images by measuring the angle of interaction between the cell and the fiber. The force vectors are easily measured in the single cell-fiber

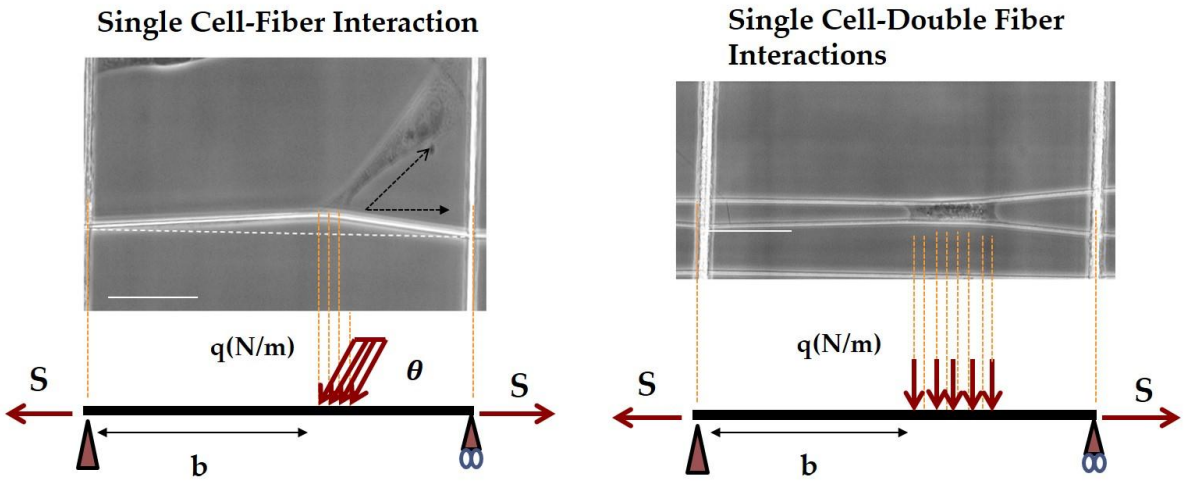

Figure 5 shows how the cell behavior is modeled. Both the single and double fiber interactions are modeled as a beam under tension with a non-uniform distributed load. A force vector is incorporated in the single fiber pull while the double fiber pull is assumed to be strictly perpendicular to the fiber.

interaction and are incorporated in the model. In contrast, the force vectors in the double fiber interactions are not obvious and are assumed to be vertical.

The deflection curve of the beam model is derived in Appendix A by using a series of sine waves to represent the beam profile. The deflections are small and remain below the elastic limit of the fiber. In addition, the diameter of the fiber was assumed to be uniform and circular. The final equation for calculating the deflection is:

$$y = \frac{2l^4 q}{EI\pi^5} \sum_{n=1}^{\infty} \frac{1}{n^3(n^2+\alpha)} \left(\cos \frac{n\pi(l_{attach}+b)}{l} - \cos \frac{n\pi b}{l} \right) \sin \frac{n\pi x}{l}$$

Where

$$\alpha = \frac{Sl^2}{EI\pi^2}$$

q is the density of the force, l is the fiber length, E is the elastic modulus, I is the moment of inertia, S is the fiber tension, b is the start of the distributed load from the left boundary and l_{attach} is the length of the distributed load.

1.8.6i Determining Constants

The elastic modulus of the fibers is assumed to be the same as the bulk value, 2.3MPa for PU (Lubrizol Data Sheet) and 3.3GPa for PS (Engineering ToolBox). The fiber length and deflection profile are taken from the experimental time-lapse images. The diameter is calculated from ESEM imaging of the fibers. The fiber tension is found from atomic force microscopy.

1.8.6ii Inverse Methods

Using inverse methods, the density of the force, the location of the load and the length of the distributed load is calculated from the experimental deflection profile as shown in Figure 6.

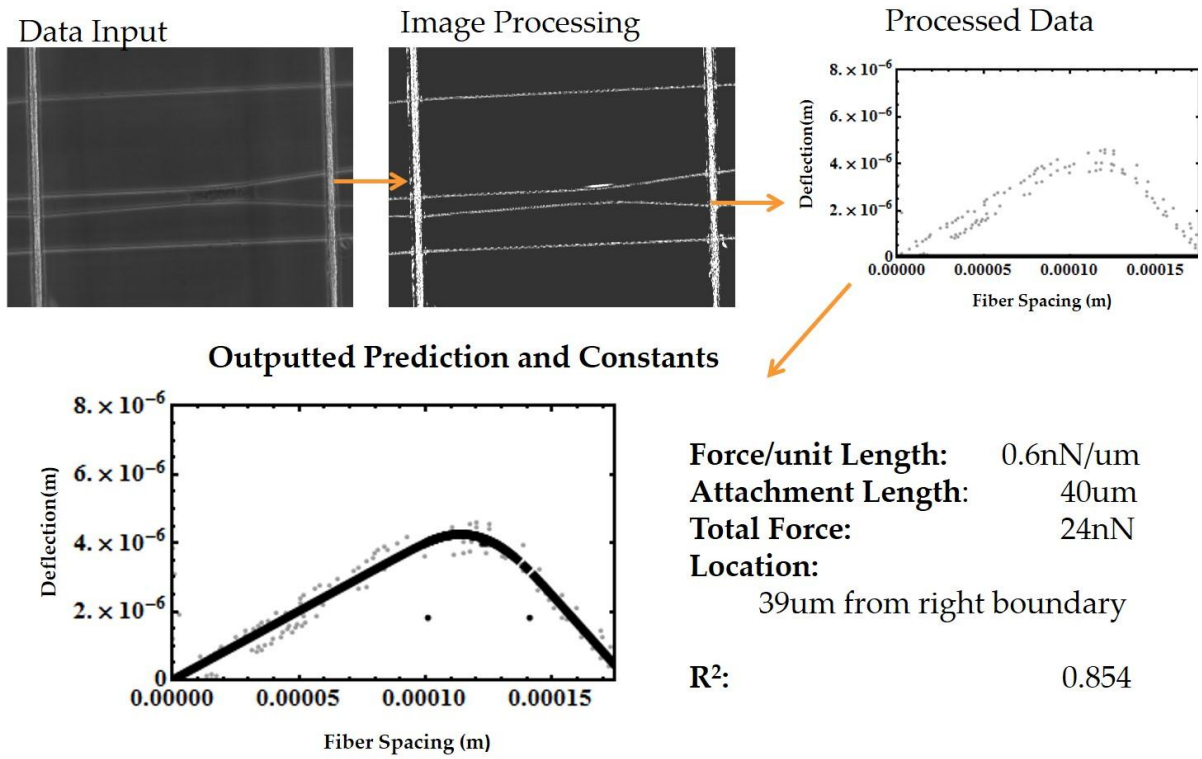

Figure 6 shows the inverse method process. 5A shows how the experimental deflection profile is inputted into the Mathematica program. The image is processed (5B) to output the deflection profile of the lower fiber as discrete points (5C). Using least square minimization, the attachment length, force magnitude and location of force is calculated and outputted by the program (5D).

The inverse method simulation works by importing individual images of the experimental cell fiber deflection into the Mathematica®. The code than separates out the beam deflection from the background and converts it into discrete points. Using a least squares minimization, the magnitude, location and length of the distributed load are solved by the program. The statistical fit of the predicted curve to the experimental curve is demonstrated by an R^2 value.

Chapter 2:

Single Cell Migratory Forces and Force Modulation

2.1 Introduction

Cells interact with a wide range of biomechanical cues such as the topography, rigidity, shear stress, hydrostatic pressure and compression in the human body. These mechanical effects determine cell behavior and are intertwined into how the cell interacts and responds to its environment. Understanding how cells sense and convert these mechanical signals into biological signals has garnered much interest as impairments of these processes have shown to be underlying causes of many diseases.[5]

Mechanical properties have been shown to change with the progression of many diseases where cancers, malaria, and sickle cell anemia have all shown mechanical changes at the cellular level. In malaria and sickle cell anemia, the invasion of the parasite or virus causes the healthy red blood cell to become stiff and cytoadherent. [6,7] In addition, the progression of cancer cells to metastasis shows a significant change in stiffness where the stiffness of the metastatic cell is 70% lower than that of a benign cell. [8,9] Furthering this knowledge brings much promises in paving new ways to diagnosing and treating diseases.

Mechanical forces are also involved in the regulation of normal cell physiology. The cell's ability to interact with its environment through attachment, cell-cell junctions or the application of loads requires the cells to sense and apply mechanical forces, which have been shown to alter gene expression and differentiation. Changes in stiffness have been demonstrated to change the lineage of mesenchymal stem cells where very stiff substrates promote osteogenesis and very soft substrates promote neuronal type cells. [10]

One mode by which the cell interacts with its environment is through the extracellular matrix (ECM). The ECM is composed of fibrous proteins ranging from 30-70nm in diameter and can form bundles ranging from 200 nm – 1 μm in diameter.[11,12,13] This fibrous microenvironment delivers direct biophysical cues

and biochemical cues to the cell. It provides biochemical cues through diffusible factors, cell-cell signaling and the reservoir of growth factors and adhesion molecules from the active part of the ECM. In contrast, ECM biophysical cues are generated through topography changes and changes in externally or internally applied stress that is commonly generated by mechanical properties of the ECM.[14]

The method by which the cell interacts with the ECM is through adhesions that link the cell to its internal actin cytoskeleton. This interaction allows the cell to generate and exert contractile forces onto the extracellular environment through the internal contraction of the cytoskeleton. [15] This contractility dictates the assembly or disassembly of the focal adhesions and is necessary for a wide range of biological processes such as differentiation and cell migration. In conjunction, the assembly of new adhesions and their development into stable adhesions determines cytoskeletal remodeling and actin polymerization. [16]

The cell's mechanical interaction with its environment has been shown to be closely related to the focal adhesion protein zyxin, which has become known as the hallmark of mature adhesion[17]. In the cell it has been shown to be essential to the cell's ability to reinforce its actin cytoskeleton in response to stress and undergo forced actin polymerization[18]. The removal of the internal contraction through mechanical or chemical means results in the delocalization of zyxin from the adhesions[19]. In addition, Zyxin null fibroblasts were unable to thicken their cytoskeleton in response to stretching. [20] Talin has also been shown to be extremely relevant protein in the interaction between the cell and the cell substrate. Talin plays the role of the anchoring protein and is required for the link between actin and integrin. Without talin the cell is unable to form focal adhesions that allow for stable attachment.

Through the advancement in nanotechnology, much progress has been made in continuing to unfold the complexities of these biophysical cues with respect to analyzing the topographical features as well as the mechanical forces that directly affect the cell. A large variety of micro-fabrication techniques have

been used to try to model the ECM architecture and adhesiveness (lithography[21], hydrogels, electro spinning[22], micro-pattering[23] to elucidate the biological mechanisms involved in dictating cell behavior. In conjunction, force measuring techniques[5] such as micropipette aspiration[24], laser trapping, magnetic probes[25,26], microcantilever-based force sensors (AFM)[27], micropost arrays[28], microelectrode arrays[29] have been used to exert and quantify the forces involved in the biological process of the cell.

These techniques have brought enormous amount of insight on the cell's mechanical microenvironment where biophysical cues such as stiffness[30,31], topography[32] and alignment are involved in determining cell morphogenesis, migration, adhesion, proliferation, differentiation and complex inflammatory cascades. [33] These techniques provide valuable and detailed insights on cellular behavior , yet are often limited to two dimensional flat surfaces which are unable to capture the three dimensional interaction of the cell with the natural fibrous ECM. Furthermore, this variation in dimensionality cannot be ignored as recent studies have shown opposing behavior in gene expression, morphology and cytoskeleton arrangement between 2D and 3D cell environments .[34,35]

In an attempt to answer these challenges in understanding the cell's mechanical response to a fibrous three dimensional environment, we propose a novel force measuring platform that provides a suspended fibrous environment for migratory cells to interact and modulate their forces. In this fibrous environment we have the conventional 2D environment but with the added dimensionality from the curvature of the fibers. The forces of these migratory cells can be easily approximated by using beam mechanics to study the cell's interaction with the fibers.

We utilized Spinneret based Tunable Engineered Parameters (STEP) technique[12] that allows us to deposit aligned suspended nanoscale fibers with control on diameter, spacing, orientation, and material. By altering these parameters, we are capable of creating unique scaffolds of not only a desired material stiffness but a more encompassing structural stiffness. Furthermore, the stiffness within a

single scaffold can be varied to create a force measuring platform where regions of very high stiffness intersect with regions of very low stiffness resulting in a simple beam with pin-pin boundary conditions which allows us to measure forces of individual migratory cells in a fibrous environment.

Using this platform, we are capable of measuring the transient force response and cytoskeleton arrangement of migratory NIH3T3s to changes in the structural stiffness of a fibrous environment.

2.2 Results

Using STEP, we were able to manufacture fibrous force measuring scaffolds of variable structural properties to analyze the cell migratory behavior. The progression of migration and the ensuing force modulation through talin, zyxin and actin localization and reorientation was studied with changes in the mechanistic structural parameters. Results showed that the combination of tension, fiber diameter and fiber geometry elicit unique force modulating behaviors.

2.2.1 Structural Properties

In this study, large diameter polystyrene was invariably used throughout the study as the fixed non-deformable boundary as a support for the deformable polyurethane fibers. By changing the spinning parameters, polyurethane fibers were manufactured from 500nm to 3 microns in diameter with tensions between 0.5μN to 10μN. In the extreme condition of large diameter and large tension, the cell cannot deform the polyurethane and is as rigid as the polystyrene support. In contrast, fiber scaffolds of low diameter and low tension, the cell significantly strains the fiber. In both cases, forces cannot be calculated using Euler beam model. Thus accurate single cell force measurement requires a balance between tension and diameter to maintain the assumptions required to use Euler beam equations. This means deflections must be small (5-10 microns) compared to fiber beam lengths between 75 microns and 150 microns in length. While following these conditions, the maximum force for NIH3T3 fibroblasts were measured with respect to beam stiffness using inverse methods highlighted in Figure 1

In addition to changes in the structural stiffness of the polyurethane fibers, we manipulate the fiber hierarchical assembly (spacing) geometry. For single cell-single fiber polyurethane interactions, fibers are deposited with a separation of approximately 100 microns to prevent cells from spreading and

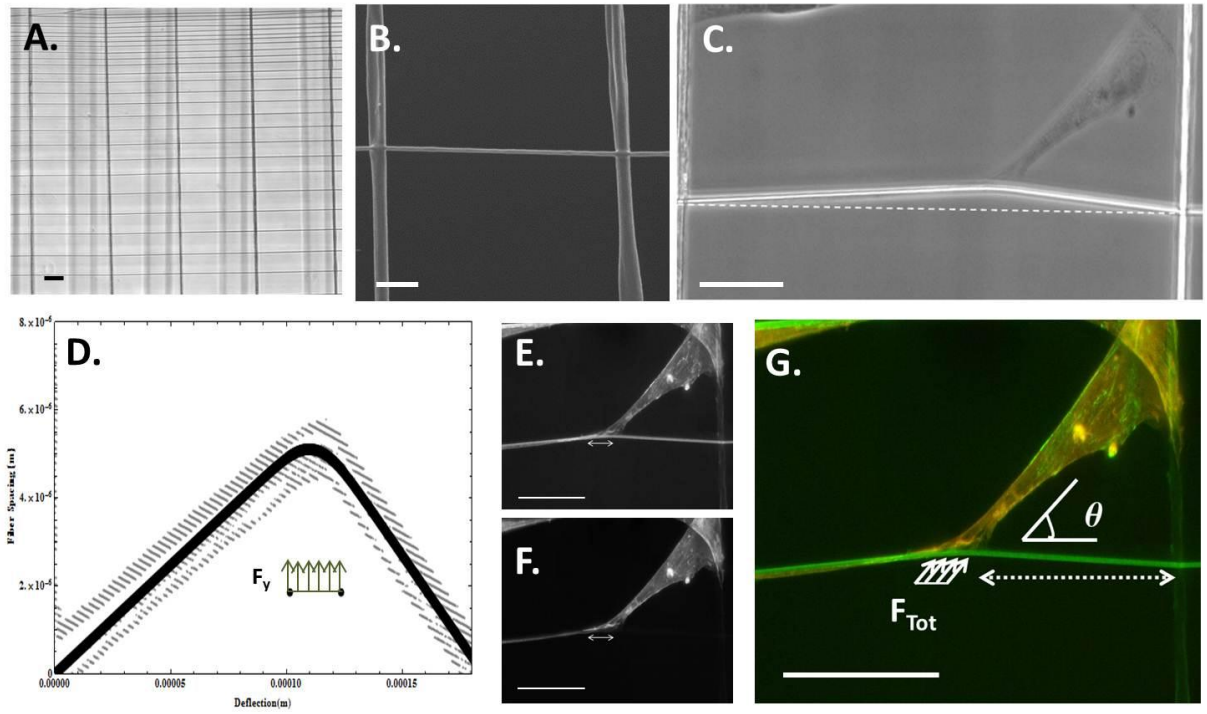

Figure 1 **shows the manufacturing and analysis of STEP enabled force measurement platform. 1A shows an ESEM image of our orthogonal fibers with large diameter PS in vertical and the deformable PU in the horizontal. 1B shows a zoomed in image of our pin-pin boundary conditions where the PU thoroughly fused to the vertical PS fibers. 1C is a phase image of a cell pulling and deflecting a horizontal polyurethane fiber. 1D shows the matched model parameters to the experimental deflection data. The model (black line) closely fits the experimental data (dashed gray lines). The solid gray dots below the fiber indicates the location and length of the predicted cell attachment. 1F shows the F-actin stain and 1E shows the talin stain which are compared to the model predictions in 1G. The predicted distributed load follows exactly with the talin expression along the length of the fiber. The angle of the talin retrograde fluxes with the deflected fiber is used to determine the force vector angle.**

interacting with multiple fibers. However, for multiple fiber-single cell analysis, polyurethane fiber spacing is varied between 5 to 30 microns where the cell can easily spread between and interact with multiple fibers. In the subsequent sections we analyze the progression in force behavior between a

single polyurethane fiber, between single polyurethane and single polystyrene fiber, and between multiple polyurethane fibers.

2.2.2 Cell Migration on Fibrous Force Platform

The cell adjusts its morphology constantly as it migrates through the force scaffold. The changes in morphology are conceptualized in Figure 2. Cells on single PS-PU fiber system spread and contract as they move towards the stiffer fiber (PS) boundary as schematically represented in Figure 2A. Figure 2B-D shows the typical cell interaction with the boundary as the cell combines with the boundary and begins migrating along the polystyrene boundary. Figure 2E-J shows a cell migrating simultaneously along the rigid polystyrene fiber and back across the polyurethane fiber whereupon the cell pulls and detaches from the fiber. Figure 2K-L shows the cell migrating from the fixed boundary onto two parallel polyurethane fibers. In this configuration the cell simultaneously contracts between the fibers as it migrates forward. All of the cell behaviors are abundant on the PS-PU force scaffolds however for force analysis; only the single pull behavior can be analyzed with our beam model (2E-J). The other force modulating behaviors are described in the future work section.

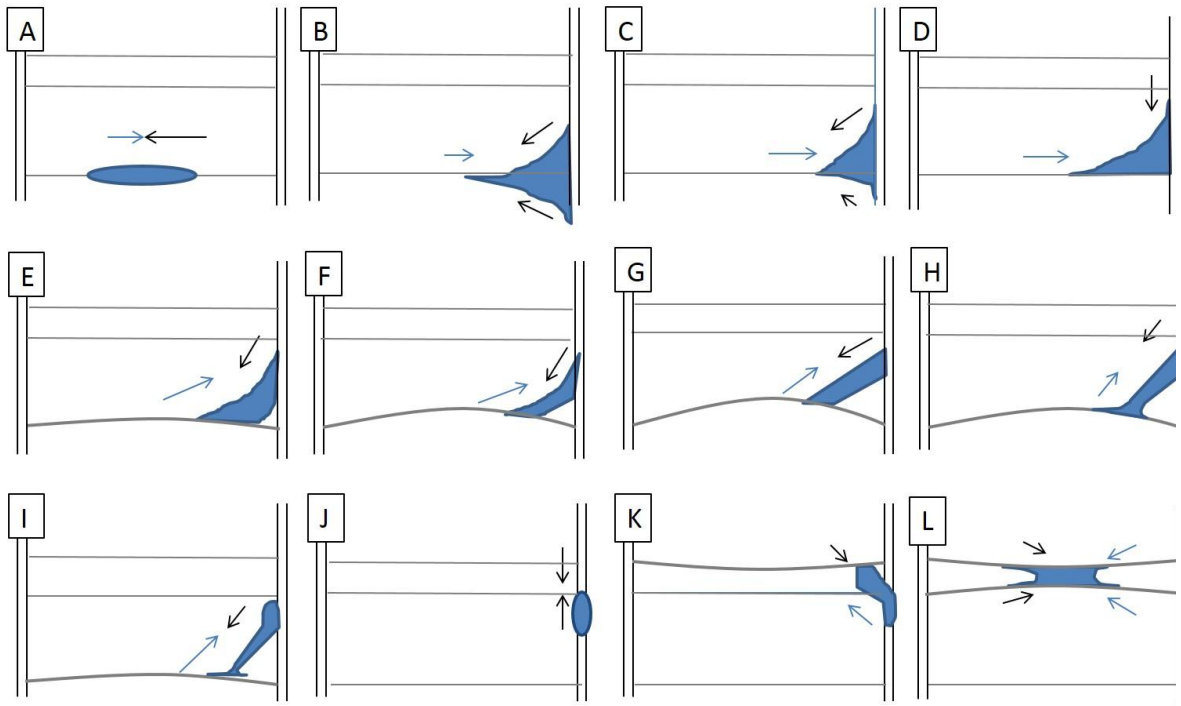

Figure 2 shows the concept drawing of the unique cell and force behaviors through our fibrous force measuring scaffold. 2A shows the initial attachment to the deforamble fiber. The cell contracts and migrates to the rigid polysytrene fiber where it spreads and uses the rigid fiber as a base to deform the polyurethane(2B-2I). As the fiber is deformed, the cell begins to detach and completely reattach to the polystyrene fiber(2G-2I).

2.2.3 Single Fiber Pull

Single cell-fiber interactions occur for a cell a contraction between a single polyurethane fiber and a rigid polystyrene fiber. This process is demonstrated in Figure 3A through a pull over 1.5 hours with the calculated model in Figure 3B. The cell begins attached to the fiber but exerts no measurable force onto the fibers. With time, the cell migrates outwards away from the rigid polystyrene fiber applying a steadily larger force with time. The cell linearly increases its force over 90 minutes (0.6nN/min) as the cell approaches a maximum force of approximately 60nN. Changes in the polyurethane mechanical properties will elicit different force magnitudes and is further explained in the next section.

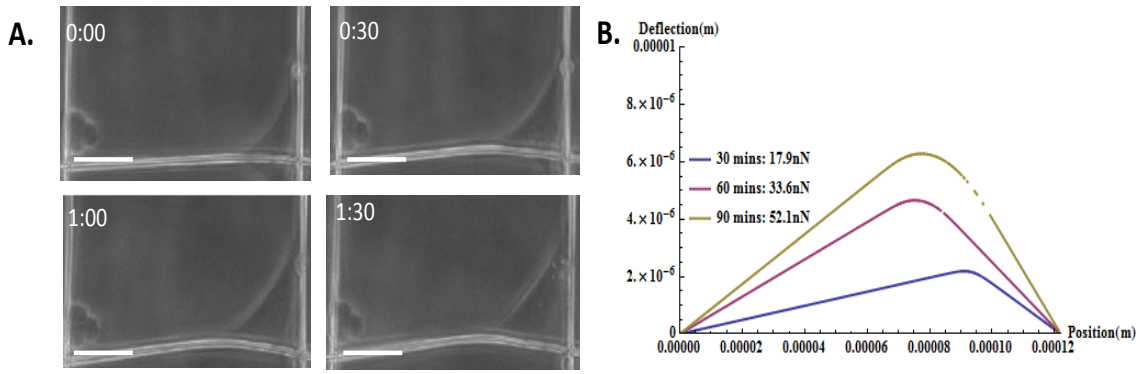

Figure 3 shows the single fiber pull behavior over 90 minutes with the model fit in 3B. The cell increases its force at a constant rate before reaching a maximum for of 60nN (3A).

2.2.4 Maximum Force Quantification

From the experimental deflection profiles, the maximum total cell force throughout the fibroblast population was calculated and related to the maximum fiber deflection, beam length and diameter. These values were measured using optical microscope images as demonstrated in Figure 4F. These parameters were plotted with the maximum calculated force in Figure 4A, 4B and 4E. The average maximum force of the NIH3T3 fibroblasts was 60nN. However, the calculated maximum cell force appears to be independent of the measured length, diameter and deflection. In addition, the maximum deflection was plotted with respect to diameter and length in Figure 4C and 4D. The deflection tends to increase with a decrease in diameter and increase in fiber length.

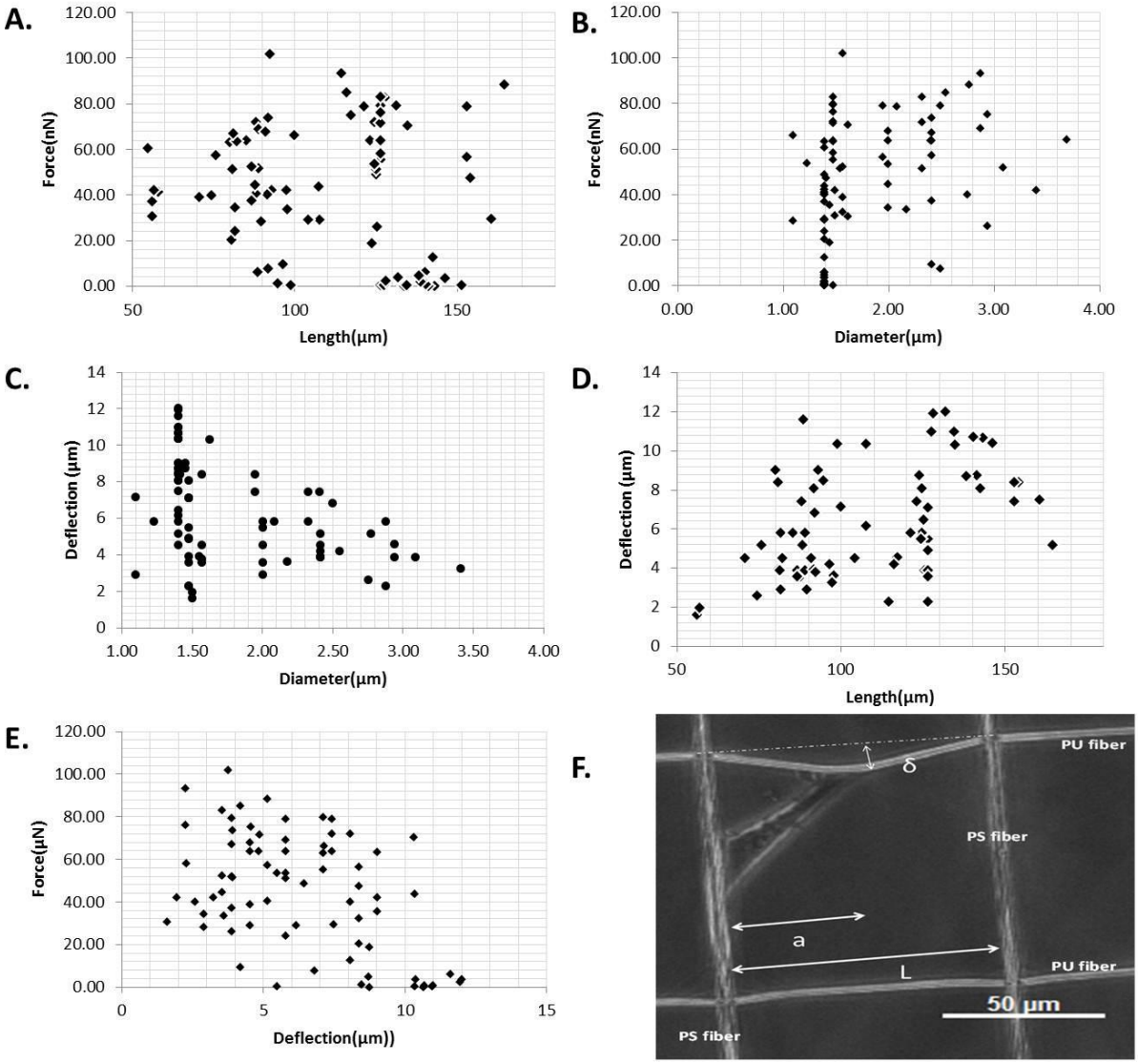

Figure 4 shows the maximum force of NIH3T3 fibroblasts plotted as a function of the fiber dimensions (4F). Force appears to be independent of Length (4A) Diameter (4B) and deflection (4E). However the maximum deflection was shown to increase with decrease in diameter and increase in fiber length which is consistent with the trends associated with a decrease in beam stiffness.

2.2.5 Attachment Length and Force Density through Detachment

Using inverse methods, the density of the force and the length of the distributed load are calculated for each cell-fiber deflection. The predicted distributed load or the calculated attachment length was plotted as the cell began to detach from the fiber in Figure 5. As the migrating cells released from the fibers, the magnitude of the force was a function of attachment length and is plotted in Figure 5A. Two different mechanisms were observed as the calculated attachment length shortened and eventually completely detached. First, as the cell detached, the exerted force decreased linearly at a rate of 0.52nN per micron. However, when the attachment length dropped in half, the detachment rate more than tripled to 1.72nN per micron.

In conjunction with changes in attachment length, the calculated force density (q) changed through detachment. Contrary to attachment length, attachment strength linearly increases with a decrease in attachment and is plotted in Figure 5B. In the cases of attachments that are greater than 35 microns, there is a negligible change in attachment strength. In addition, the extrapolation of the intersection of the attachment strength line with the y-axis indicates there is a ~3.2nN force at 0 attachment length. This is the result of a single point attachment and most likely indicates the maximum strength of a single adhesion but this requires further investigation.

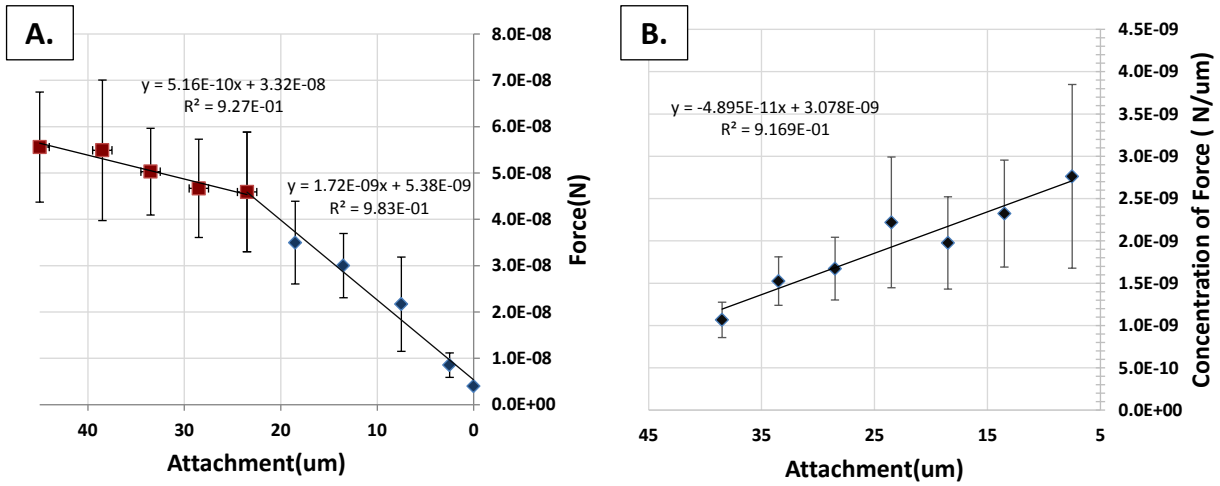

Figure 5 shows the detachment behavior of the cell with respect to attachment length. Force decreases linearly at .5nN/um until approximately 25 microns where the force decrease rises to 1.7nN/um. Figure 5B shows that with fiber detachment the concentration of the force increases linearly where it maxes out at approximately 3nN before complete detachment.

Preliminary actin stains suggest the attachment length behavior occurs because of the remodeling of the actin structure to more aligned configuration in the direction of the stretch. Our preliminary analysis on live focal adhesion dynamics the change in force density is caused as a result of focal adhesion strengthening However, further investigation is required to fully understand the force mechanisms.

2.3 Future Work

Alternatively to the single pull behavior, force behavior can be elicited with different cell fiber interactions in the form of single fiber interaction and double fiber interaction. These interactions are more biologically relevant but are more difficult to model than the single pull behavior. Studying and characterizing these morphologies should be the next step in the force platform development.

2.3.1 Single Fiber Attachment

After the cell's initial attachment to a single polyurethane fiber (Figure 6A), the cell spreads and is able to contract low structural stiffness fibers. Larger diameter fibers typically cannot be strained but as the diameter decreases the cell can axially strain the fiber to a larger degree. The progression of contraction on the fiber is shown at different positions in time. The cell attaches to the fiber at its extremes. As the cell migrates forward along the fiber, the cell pulls at its extremes and strains the fiber inwards along the axis of the fiber. The leading edge pulls the fiber at a faster rate than the trailing edge causing the fiber to slack within the cell and lose tension). The slacked fiber is coiled and pushed to the periphery of the cell. This process is shown conceptually in Figure 6B.

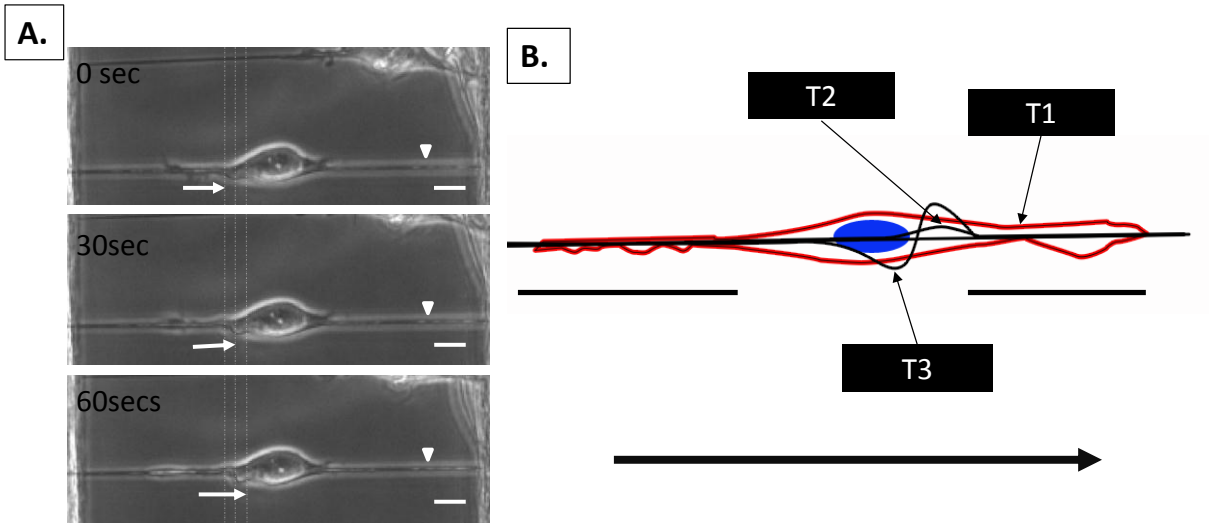

Figure 6 shows the preliminary results of the cell's attachment and force modulation to a single polyurethane fiber. 4A shows the progression of the cell pulling and coiling the fiber in the cell interior. Figure 6B is a concept drawing showing that the fiber remains in tension outside the cell boundaries and along the edges of the cell. However, in the inteiror, the fiber loses tension as the fiber slacks in the interior becomes of the rapidelongation and stretching of the fiber through the lamellapodia.(Scale bars: 20 microns)

2.3.2 Double Fiber Contraction

Cells migrating between two parallel fibers have been shown to contract between the fibers allowing for force calculation through this unique morphology shown in Figure 7. Figure 7A shows the phase image

of the cell contracting the two fibers. Figure 7B shows the cytoskeletal stain of a cell during double contraction. Preliminary talin stains show aggregation along the length of the cell-fiber interaction. In addition, preliminary results show the forces perpendicular to the fibers are equal and opposite to each other. As result, finding the force vectors of the cell-fiber interaction are required to fully understanding the cell's method of migration.

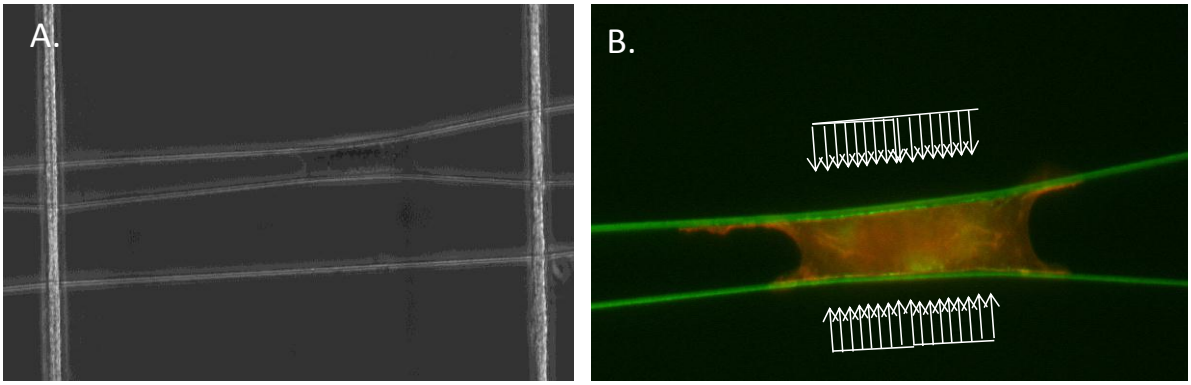

Figure 7 shows the preliminary double fiber contraction behavior. 7A shows the phase image of a cell migrating along two parallel fibers. 7B shows the cytoskeletal stain and proposed modeled load.

Chapter 3:

Wound Healing Assay

3.1 Introduction

The body has a natural process to heal injuries or breaks to the skin surface. This process known as the wound healing, involves a complex sequence of events that consist of inflammation, tissue repair and tissue remodeling.[36]

Immediately after a wound is formed, inflammatory cells are recruited to damaged tissue to sterilize the wound. This triggers the rapid proliferation of fibroblasts that enables tissue growth by laying down ECM proteins. Circulating progenitor cells migrate to the injured tissue triggering rapid cellular proliferation causing the formation of new blood vessels and epithelium. This initial growth last between 2-10 days before transitioning to the remodeling stage which can last as long as a year. During remodeling the tissue is further strengthened and reorganized until the healing process is complete.[37]

This natural process is not perfect in adult humans. After a year of remodeling, the repaired wound commonly leads to a non-functioning mass of fibrotic tissue with a tensile strength of 70 – 80 % of the original undamaged tissue. Scar formation ultimately results from excess accumulation of an unorganized extracellular matrix where normal extracellular matrix architecture is never fully achieved. Pathological scars such as keloids and hypertrophic scars occur when the normal wound healing process goes into over drive and results in an excessively disorganized collagen layer, these scars are raised, cosmetically unpleasing, and associate with symptoms such as pain and itching. [38]

In order to address these issues and to further understand this complicated process, wound healing assays have been used for detailed cell biological studies of wound repair specifically looking at cell polarization, matrix remodeling, cell migration and many other processes. Typical wound healing assays are conducted by making an incision to a cultured cell monolayer on a coverslip or multiwall plate. After incision the collective cell migration and reclosure of the monolayer is monitored until complete wound closure.[39]

This technique is very cost effective and avoids the use of expensive and time consuming animal models. However, there are multiple drawbacks to this technique. One the physical scratch process involves a mechanical injury to the cells resulting in a release of cellular contents into the surroundings that is highly uncontrollable. Two, modifying the surface using extracellular matrix (ECM) coatings is challenging because the scratching process might break the underlying coating.[40] Finally, the largest drawback of this analysis is these experiments are conducted on a 2D surface and does not represent the native in vivo environment.

These models are limited to two dimensional flat surfaces which do not represent the three dimensional interaction of the cell with the natural three dimensional fibrous ECM. Furthermore, this variation in dimensionality cannot be ignored where recent studies have shown behavior in 2D and 3D cell environments to be completely different with regard to gene expression, morphology and cytoskeleton arrangement.[3435] Furthermore, geometric parameters such as fiber alignment and orientation have been shown to guide and increase the migration of the cell. [414243] Cells on fibers have distinct behaviors from their flat counterpart and as a result, incorporating these biophysical factors are necessary to understand and enhance the wound healing process.

New biopolymers and fabrication techniques are also being explored as a means of enhancing this natural process with the ultimate purpose of decreasing healing time and leaving the best aesthetic repair. In order to achieve this, modern wound healings solutions try to maintain an ideal environment to facilitate cell regeneration without causing further damage to the wound or patient.[44].

Wound dressing biomaterials composed of nanofibrous mats perform two functions: One they temporarily provide a substitute for the native ECM and act as potential carrier system for the controlled delivery of antibacterial agents and other wound healing enhancers. Second, they have been shown to reduce scarring by giving cells a roadmap for tissue repair. Electrospun polymeric membranes

are currently the most advanced wound dressing material as compared to other modern bandages such as hydrocolloids, hydrogels, and alginates. [45]. They give a degree of control of the fiber deposition and can be incorporated with antibacterial components. For example, water soluble electrospun gelatin fiber mat loaded with antibacterial drugs can easily dissolve and deliver the drug when coming into contact with an aqueous medium.[46] However, a major drawback to electrospinning is the inherent instability caused by the charged jet. This instability often adds a degree of randomness to the orientation of the woven formed fibers which traditionally does not provide cells aligned pathways for faster and directed migration. In this regard, the next milestone for this platform is developing and improving the alignment of the electrospun fibers .[4]

In this study, we demonstrate the capability of using pseudo dry-spinning methods to create highly aligned polymeric nanofibers arrays at user defined geometries with a control on fiber spacing in single and multiple layers. The uniqueness of this technique removes the inherent difficulty in the electrospinning process by eliminating the charged jet. This allows us to still maintain fibers lengths in the mm to cm range while having parallelism of 2.5 degrees or less but provides us with a very high control of spacing in the micron to submicron scale.[21]

Utilizing this fiber manufacturing platform we developed a unique wound healing assay which incorporates highly controlled polymeric fiber geometries in the study of wound closure. In this assay, we analyze the migration of two opposite confluent cell reservoirs migrating onto aligned suspended fibers as a representation of fibers to guiding healthy cells into the damaged wound tissue. Unlike, typical wound healing assays, the addition of fibers activates closure and no incision or scratch is necessary to conduct the study. This removes possible factors such as ECM or cell damage effecting closure behavior.

3.2 Materials and Methods

STEP (Spinneret based Tunable Engineered Parameters) technique utilizes polymer solutions to deposit fibers of a desired diameter on a chosen substrate. A polymer is dissolved in a good solvent, one with a low evaporation point, and extruded with a micropipette. The pipette is held fix as the solution is extruded onto a translating rotating substrate of a desired geometry. As the solution is evaporated, the polymer is deposited onto the substrate. The fiber separation can be controlled by the speed of rotation and the translation speed. The result is aligned fibers of a desired length, separation, orientation and diameter. Polymer solution of 3% (w/w) poly(lactic-co-glycolic) acid (PLGA) dissolved in chloroform was prepared and spun using STEP technique to achieve deposition of highly aligned uniform suspended fibers (app. 400nm diameter) shown in Figure 1D. The PLGA was provided by Purac with a copolymer ratio of 85:15.

Two plastic coverslips were seeded with NIH3T3 fibroblasts, a cell line heavily involved in the wound healing process, and cultured in DMEM with 10% FBS for 1.5 weeks until a multilayered fibroblast surface formed over the two coverslips (Figure 1B). The PLGA fiber scaffolds were then applied to bridge the gap between the two separate monolayers. Figure 1A shows the method of application of the fibers directly onto the cells and the result is shown in Figure 1C. This setup creates a suspended fibrous region approximately 300microns above the underlying surface and 1.5 mm in length to study the closure mechanics of the fibroblasts (Figure 1E). Time-lapse microscopy was started once cells from the monolayer began migrating into the gap now bridged by the nanofibers. These fiber scaffolds were imaged for approximately a week until a confluent layer of cells covered the entire fiber scaffold. Media was replenished every other day during the one week time lapse.

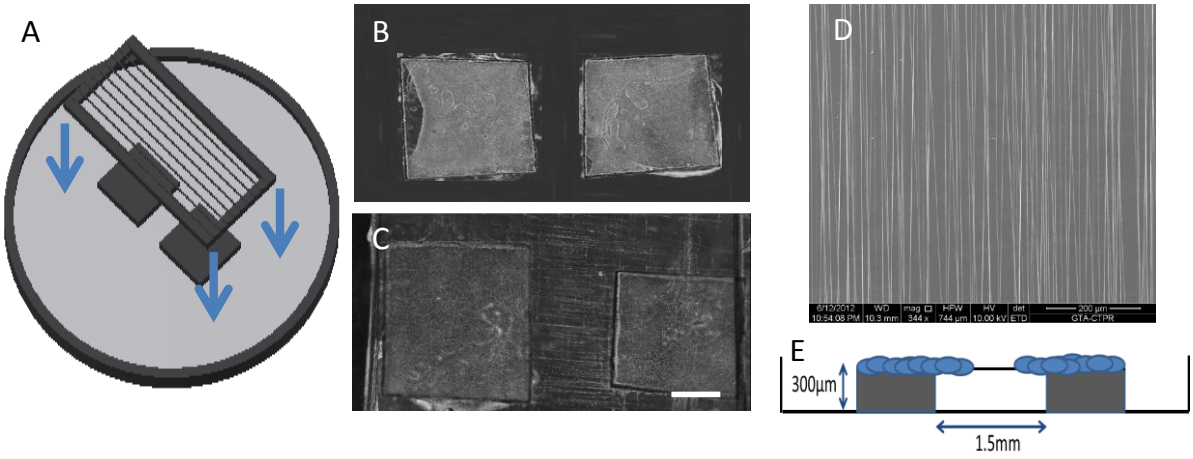

Figure 1 shows the preparation and implantation of the wound healing assay. 1A shows the conceptual schematic for the preparation of the wound healing assay, 1B shows a phase image of the cultured fibroblast before fiber implementation and 1C shows after fiber implementation. 1D is an SEM image of the aligned along the fibers between coverslips separated by 1.5mm suspended 300 microns above the underlying flat surface. PLGA fibers with an average diameter of 400nm. Figure 1E is a conceptual cross sectional view of the assay. The cells migrate

3.3 Results

The use of aligned fibers between the monolayer gaps provides a pathway for the cells to migrate and eventually fill the previously empty space between the two monolayer covered substrates. These cells are completely suspended and are supported only by the fibers and the bonds formed with their neighboring cells. This process occurs in two principal steps, axial migration, where cells emerge and migrate along the fiber, and gap closure where cells fill in the space between the fibers.

The onset of cells is dictated by the pathway provided by the addition of fibers. The cells now provided with a route, will migrate from highly confluent monolayer to the low or nonconfluent fibers. This is further demonstrated by individual cells that come into contact with dense trailing groups of cells, change direction and migrate toward the less confluent area.

Multiple experiments of our wound healing model were conducted to optimize concepts for potential sutures. These experiments consisted of a two fiber types, single layer fibers and double layer

orthogonal fibers. Closure behavior was shown to vary with each set of fiber geometries and was optimized for healing. In addition we look at both the large scale migration and gap closure of the entire cell population as well as the small scale individual cell migration during closure.

3.3.1 Full Scale Closure

We analyzed two specific fiber morphologies, single layered parallel fibers and double layered orthogonal fibers and studied their effect on closure behavior. The single layered fibers and double layered scaffolds were applied to our wound healing assay with an average spacing of 50 microns

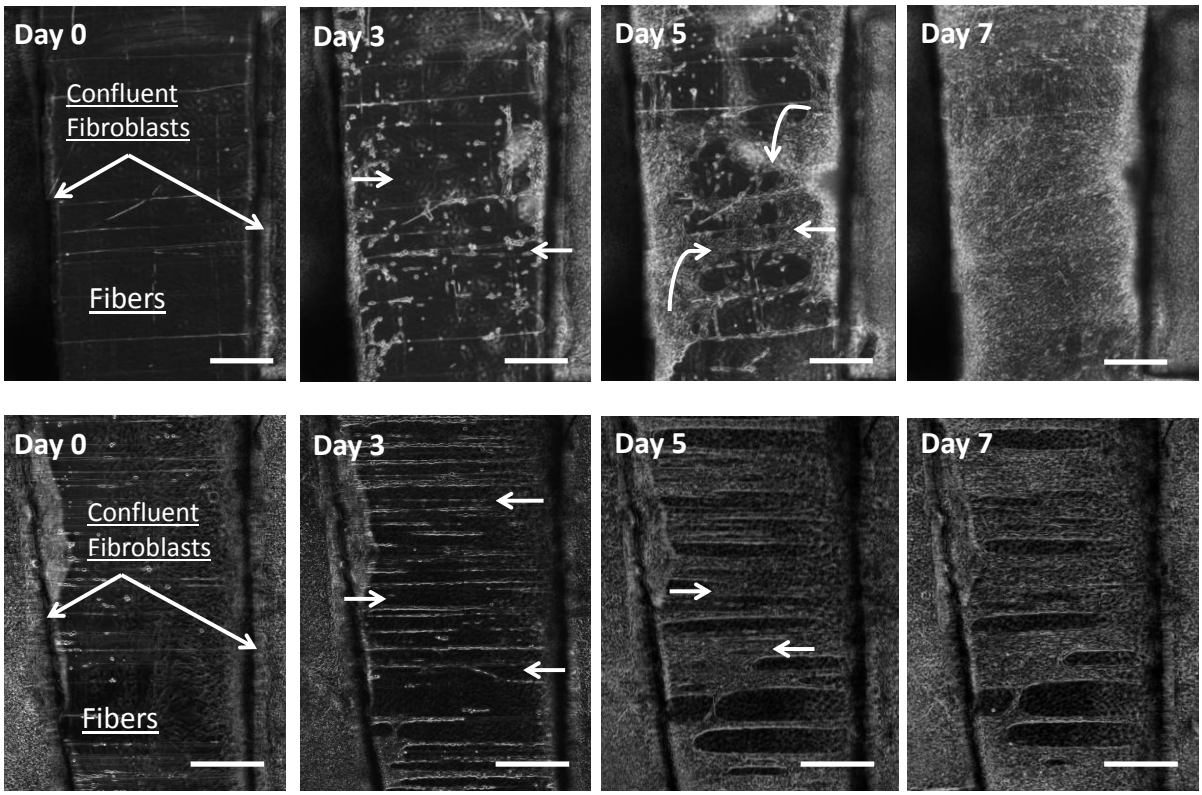

Figure 2 shows the closure behavior on double(top) and single(bottom) layered fibers at day 0,3,5, and 7.After one week the double layered fibers showed complete but the single layered fibers showed incomplete closure after one week where covular gaps remained in between the fibers.

between the fibers. In Figure 2, images at day 0, 3, 5 and 7 are shown for the double suspended (top row) and the single suspended (bottom row). On double suspended fibers, the closure occurred in multiple directions where the cells had multiple avenues to migrate onto the fibers. However, on single suspended fibers the cells' ability to migrate is limited to the single axis of the fibers. This limitation in paths for the cells to migrate caused a decrease in closure that is demonstrated by the presence of gaps at day 7 of the single suspended fibers and the lack of gaps present at day 7 of the double suspended fibers

3.3.2 Rate of Closure

Every 24 hours, the percent closure of the suspended fibers was measured for both fiber morphologies and plotted in Figure 3. Nearly all the double suspended samples showed complete closure while the single suspended samples showed on average only 60% closure over the 8 day time span. Initial closure over the first couple days was very similar between the two geometries but after day 3, there is a significant difference between the double and single fiber samples. This most likely occurs because the added fiber dimension begins to affect the closure behavior. Between day 4 and day 5 both samples demonstrated a peak closure speed but the double layer's peak was twice as fast (27%) as the single layer (13%) over the 24 hour time-span. From day 5 through 8, the double layered closure speed gradually slowed until the sample was completely closed by day 8. In the single suspended samples, closure rate stayed consistent until there was a slight drop off by day 8.

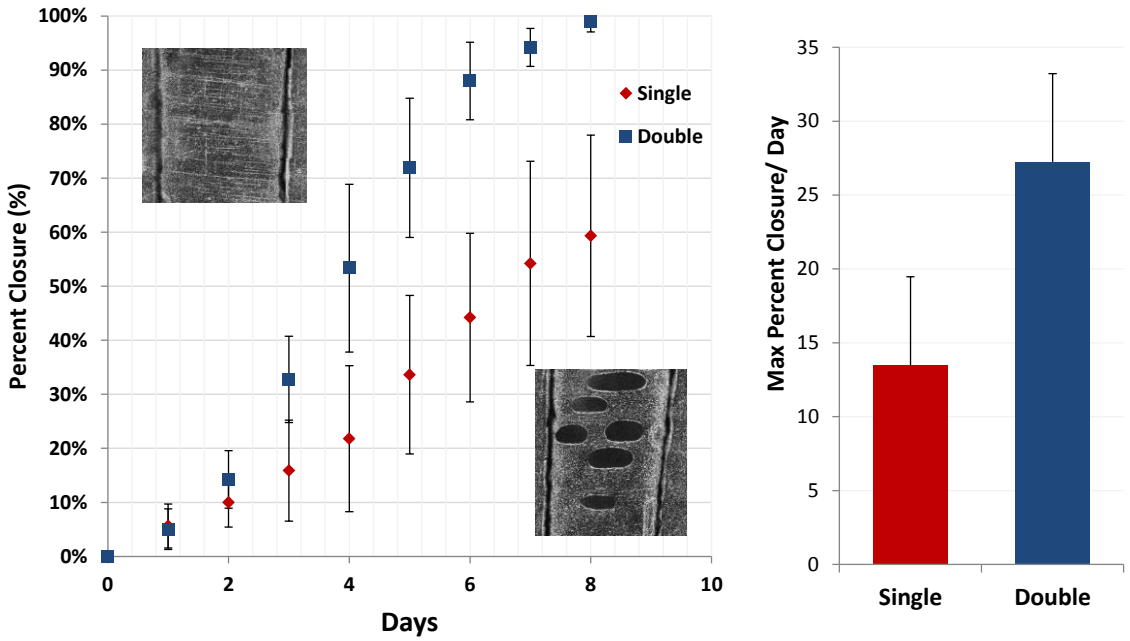

Figure 3 shows the percent closure each day of the experiment. The double layered fibers showed complete closure while the single suspended reached only 60% closure after one week. Peak closure rate occurred at Day 4 for both fiber morphlogies but the double layer was twice as large as the single layer. (N= 6 for each morphology)

3.3.3 Local Closure Mechanism

Closure is initiated by the bridging of the cell reservoirs by the implementation of the fiber scaffolds. Leading cells emerge as single cells that accelerate out at an average speed of ~50um/hr. These cells often switch directions and in doing so change their speeds. Each subsequent cell that follows these initial cells showed a decreased velocity and was attached to their neighboring cells forming a wave of bounded cells. These waves of cells completely cover the fibers. As these cells consume the space provided by the fibers, the pressure caused by the squeezing of the trailing cells pushes the cells off the fibers.

This process allows the cells to close the gap between the fibers. In circumstances where the fiber separation is less than 20 microns, cells can easily migrate and fill the space between the fibers. However, as fiber separation increases above 20 microns, the cells cannot easily fill the gap between the fibers and requires the coordination of migrating and proliferating cells circumventing the gaps between the fibers.

In our application of aligned parallel fibers, closure between large fiber separations (>20um) is initiated either by the perpendicular intersections formed between the fibers and the substrate or by intersecting fibers. These intersections allow the cells to build upon each other to fill the gaps between the fibers. These cells are suspended above the underlying plate and are supported only by the bonds formed with their neighboring cells. Closure between fibers can only be initiated at cell monolayer-fiber intersections of 90 degrees or less or at the fiber/substrate boundary. Cells will not migrate into the fiber gap unless the cell is pushed from the fiber. This push only occurs when there is no space on the fibers to migrate and there are high density of packed trailing cells to push the cell into the gap.

The initiation of the closure mechanism is illustrated in Figure 4. Cells migrating along the fibers are pushed off the fibers but remain in plane by its attachment to their neighboring cells. The first cells to be pushed off the fibers are the “key” cells (Figure 4A) that are able to elongate and spread between the corners of the cell monolayer-fiber boundaries forming a triangular morphology. The key cell acts as a platform that allows trailing cells to move into the gap where the trailing cells can elongate and attach equally between the fibers and the key cells. This process persists where each ensuing cell will build on top of and spread equally between the previously attached cells, eventually producing a curved suspended boundary between the fibers. This building process ceases once the angle between attached cells is too large (greater than 160 degrees) to spread and attach to the previous layer of cells and the whole monolayer then progresses forward. (Figure 4B-D)

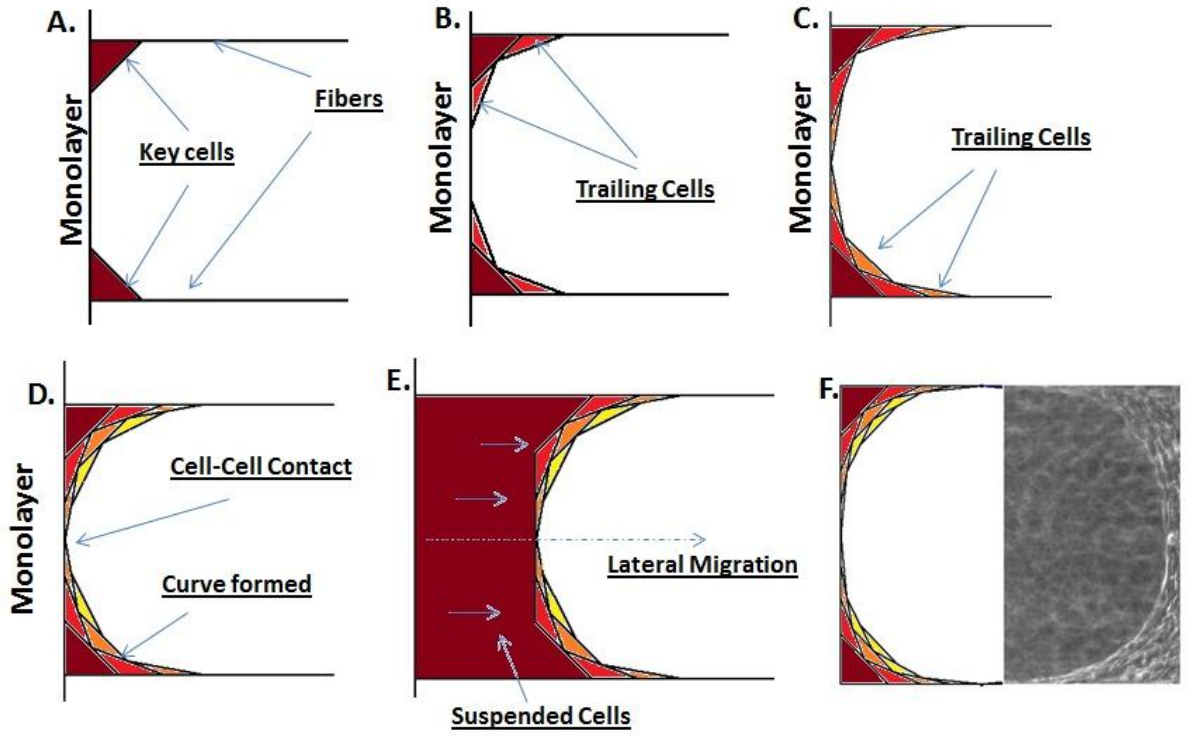

Figure 4 shows the mechanism by which the cells close the gaps between the fibers. 4A) closure is initiated by key cells that act as a platform for trailing cells (4B-C) to migrate off the fibers into the gap. This process leads to a fully developed curve (4D) that forms between the fibers. This provides the basis for lateral migration (4E) where the entire boundary moves forward, filling the suspended space between the fibers. (4F) matches the conceptual model to the actual curve formation.

The cells on the boundary or periphery of the curve provide tension that supports the now suspended cell population. Once this forms, continued gap closure from the fiber/substrate junction is advanced by the proliferation and migration of the interior cells, not by cells migrating along the edge of the curve. The continued growth of the cell population leads to an insufficient amount of space for the interior cells, forcing the boundary forward, driving the closure mechanism (Figure 4E). Despite the inward push from the interior cells, the shape of the outside boundary maintains it curve as it moves inwards away from the intersection. However, closure behavior changes when the curve comes into contact with another neighboring opposing advancing front of cells as shown in Figure 5. Complete gap closure occurs inward radial merging of the two cell fronts causing an ever decreasing an ovular hole. This

combination leads to a transition from the interior cells only pushing on the boundary laterally to the interior cells pushing inwards to close the hole. As the hole becomes smaller, single cells are cable of

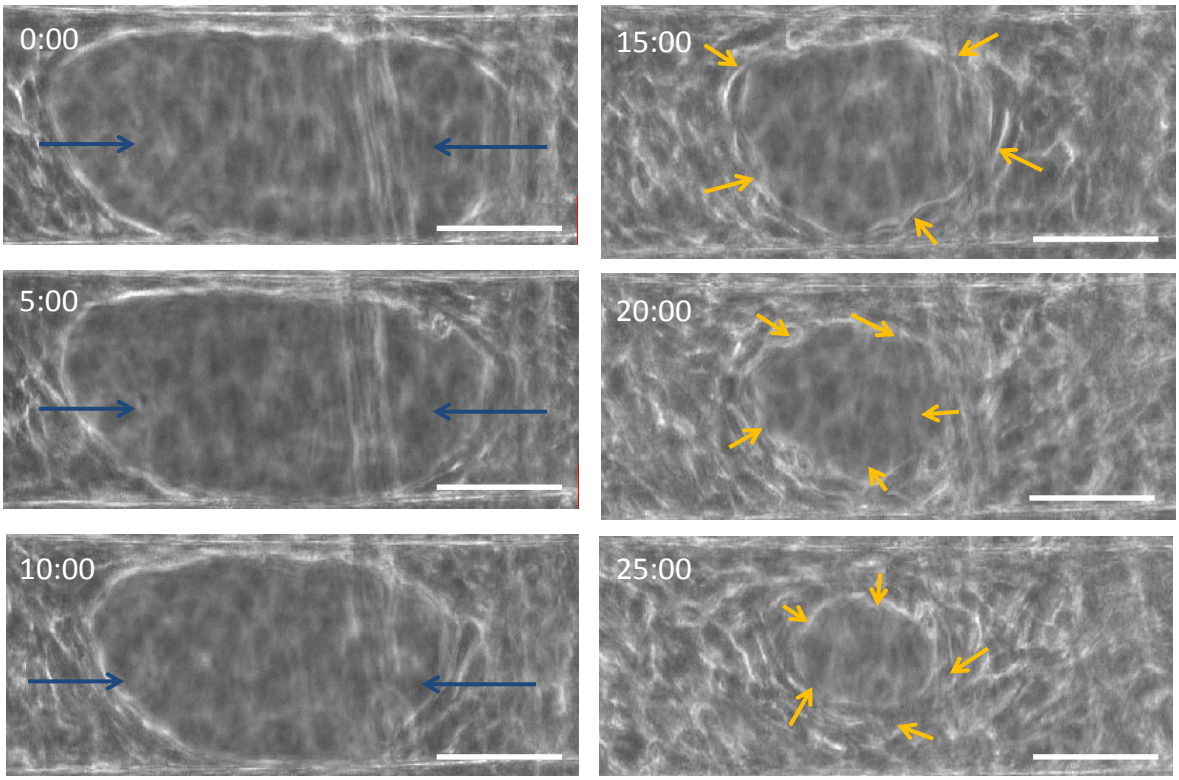

Figure 5 shows the process to complete gap closure. The boundaries from opposite sides laterally migrate together, parallel to the fibers. However, once the two boundaries come into contact with one another, the closure behavior changes from lateral closure to radial closure. In radial closure, the cells migrate from the entire length of the boundary and eventual leads to complete gap closure

bridging the gap themselves leading to complete closure.

The rate of radial closure is relatively constant throughout the entire process. The measured decrease in area is shown in Figure 5 was measured to be approximately closing at the rate of 250micron^2/hour. This value does not change between the transitions from lateral to radial closure. This value does decrease as it approaches complete closure, most likely the result of a larger force required to final close the gap.

3.3.4 Fiber Separation

The fiber separation plays a key role in the shape and development of the curve. Figure 6A-D shows curve formation between fibers separated between 20 to 100microns. With smaller fiber separations and fewer cells migrating into the boundary, the cell-to-cell angle is much smaller. Conversely, as fiber separation increases, the cell-cell attachment becomes more gradual where the average angle between the cells becomes larger and more cells are involved in the development of the curved boundary. The angle of the cells at the center of the curve is plotted in Figure 6F.

In addition, the speed at which closure occurs is dependent on the separation of the fibers. As mentioned before, cells separated by 20 microns or less, are capable of bridging the gap between the fibers without the aid of other cells and migrate at a rate of 40 microns/hr. However, as fiber separation increases above this threshold, the speed of the lateral closure decreases exponentially as shown in Figure 6E. Cells are capable of closing gaps upwards of 200 microns but can only close it at rate of 1 micron/hour much slower than the cells migrating at 40 microns/ hour along the fiber. Minimizing this separation is key to optimizing closure time.

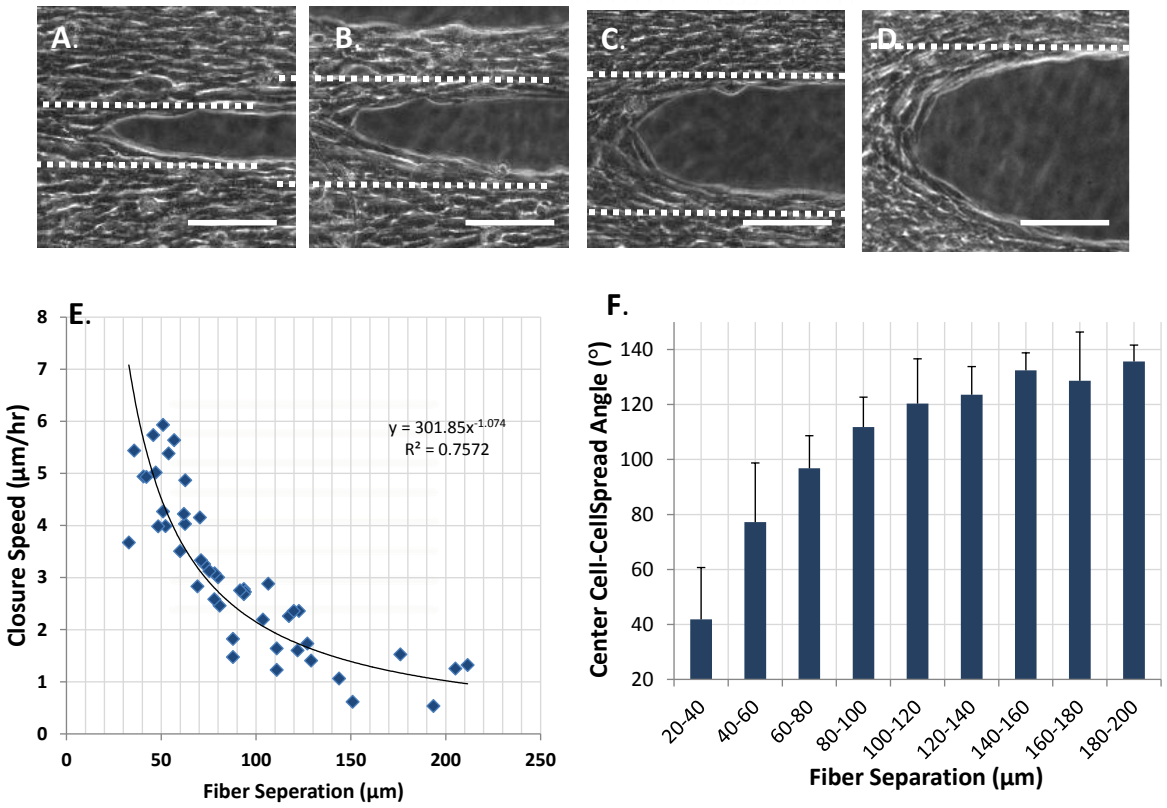

Figure 6 shows the fully developed curve with increasing fiber separations (6A-D). As the separation increases, more cells are required to form the boundary (6F) (N=75) and as shown in 6E, the closure speed decreases

3.4 Discussion

Recent advances in manufacturing techniques have allowed for the generation of biomaterials with micro or nano-sized features that are ideally suited for the study of cellular behavior. Experiments have shown that the cell's shape and function will conform to the topography of its environment where cells on nano-grooves show a high degree of alignment and migration along the grooves. Furthermore, cells on uniaxial and axially aligned electrospun fibers migrate faster than those on randomly aligned fibers. This well-established cellular behavior shows the ability to utilize alignment to direct and enhance cell

migration to a target area i.e direct healthy cells into a damaged region in the body. In our study, we show in addition to the role of alignment, fiber geometry and spacing play key roles in migration and can be utilized to optimize migratory behavior. In addition, closure between the gaps between suspended fibers elicit unique cell to cell interactions that are not present in current migration assays.

Through our optimization, orthogonally aligned fibers show an increase closure rate over uniaxial aligned fibers over an eight day study. During the first couple of days there is an insignificant difference but as the added dimension becomes more prominent, the added avenues for closure significantly enhance the closure rate by nearly two-fold. In addition, fiber spacing changed the closure rate, where fibers separated by more than 20 micron showed significantly lower closure rate than that of fibers spaced by fibers lower than 20 microns. This represents the separation by which cells can reach between multiple fibers and allows them to close the gap faster.

In situations where the fibers are spaced by gaps larger than 20 microns, closure depends on the cells ability to bridge the gap collectively where cell-cell junctions allow the cells to migrate into the gap. The larger the separation the more cells are required to bond together to interact and eventual close the gap. As more and more cells are required the rate of closure decreases.

We demonstrate a new way of analyzing the group cell migration on suspended fibrous scaffolds. The suspended fiber networks present a closer representation of the native fibrous environment than that of typical scratch assays. We show unique closure behavior in response to changes in geometrical cues such as fiber orientation and spacing. In addition the suspended nature of the biodegradable PLGA fibers allows for the possible use in future sutures where scaffolds should have a fiber spacing of under 20 microns with an orthogonal configuration.

3.5 Conclusion

This wound healing assay revealed closure behavior is dependent on the cell's interaction with its physical environment. The added dimension of the double layered orthogonal fibers compared to the single layered fibers showed much faster and complete closure. In addition the separation of the fibers played keys roles in how the cells behaved and interacted with one another during closure. Closure was maximized at fiber separations of 20 microns or less where the cells could easily migrate between fibers.

Chapter 4:

Conclusions and Future Directions

In conclusion, we have demonstrated a wide range of applications for our aligned fiber network in the study of cell biology. This was achieved both by developing a force measuring platform of our single cell behavior as well as a group migration assay studying the cell-cell interactions during closure. This thesis demonstrates unique cell morphologies and attachment behaviors along our fibers that are not present in previously reported technique or platforms.

The next step from this thesis would be to further develop the double contractile behavior as well as the single fiber buckling behavior as these are more biologically relevant force behaviors than that of our current single pull analysis. In addition, the force measuring platform should be developed into higher throughput system to allow for the use as a diagnostic system.

With respect to the wound healing assay, the next step should be further understanding the effect of mechanical properties on group cell migration with respect to stiffness, spacing and geometry. In addition, further time should be invested in understanding the mechanisms of the cell-cell interaction that allow for the suspended closure. Specifically, the actin arrangement, focal adhesions and the gap junctions should be studied to further understand the closure process.

Finally, I would like to acknowledge STEP lab for all of their help and support to complete these experiments and I wish them the best of luck in their future endeavors. In addition, I would like to thank the committee members for their time reading and improving upon the thesis.

References

1. Nain, A.S., Sitti, M., Jacobson, A., Kowalewski, T. & Amon, C. Dry Spinning Based Spinneret Based Tunable Engineered Parameters (STEP) Technique for Controlled and Aligned Deposition of Polymeric Nanofibers. *Macromolecular rapid communications* **30**, 1406-12 (2009).

2. Nain, A.S. *et al.* Control of cell behavior by aligned micro/nanofibrous biomaterial scaffolds fabricated by spinneret-based tunable engineered parameters (STEP) technique. *Small (Weinheim an der Bergstrasse, Germany)* **4**, 1153-9 (2008).

3. Shin, Y.M., Hohman, M.M., Brenner, M.P. & Rutledge, G.C. Experimental characterization of electrospinning: the electrically forced jet and instabilities. *Polymer* **42**, 09955-09967 (2001).

4. Pan, H., Li, L., Hu, L. & Cui, X. Continuous aligned polymer fibers produced by a modified electrospinning method. *Polymer* **47**, 4901-4904 (2006).

5. Kim, D.-H., Wong, P.K., Park, J., Levchenko, A. & Sun, Y. Microengineered platforms for cell mechanobiology. *Annual review of biomedical engineering* **11**, 203-33 (2009).

6. Park, Y. *et al.* Refractive index maps and membrane dynamics of human red blood cells parasitized by Plasmodium falciparum. *Proceedings of the National Academy of Sciences of the United States of America* **105**, 13730-5 (2008).

7. Lee, G.Y.H. & Lim, C.T. Biomechanics approaches to studying human diseases. *Trends in biotechnology* **25**, 111-8 (2007).

8. Suresh, S. Biomechanics and biophysics of cancer cells. *Acta biomaterialia* **3**, 413-38 (2007).

9. Physical, O., Take, S. & Cancer, O.N. The forces of cancer. 6-7

10. Engler, A.J., Sen, S., Sweeney, H.L. & Discher, D.E. Matrix elasticity directs stem cell lineage specification. *Cell* **126**, 677-89 (2006).

11. Mammoto, T. & Ingber, D.E. Mechanical control of tissue and organ development. *Development (Cambridge, England)* **137**, 1407-20 (2010).

12. Ottani, V. *et al.* Collagen fibril arrangement and size distribution in monkey oral mucosa. *Journal of anatomy* **192 (Pt 3**, 321-8 (1998).

13. Bozec, L., van der Heijden, G. & Horton, M. Collagen fibrils: nanoscale ropes. *Biophysical journal* **92**, 70-5 (2007).

14. Kim, D.-H., Wong, P.K., Park, J., Levchenko, A. & Sun, Y. Microengineered platforms for cell mechanobiology. *Annual review of biomedical engineering* **11**, 203-33 (2009).

15. Parsons, J.T., Horwitz, A.R. & Schwartz, M. a Cell adhesion: integrating cytoskeletal dynamics and cellular tension. *Nature reviews. Molecular cell biology* **11**, 633-43 (2010).

16. Ridley, A.J. *et al.* Cell migration: integrating signals from front to back. *Science (New York, N.Y.)* **302**, 1704-9 (2003).

17. Zaidel-Bar, R., Ballestrem, C., Kam, Z. & Geiger, B. Early molecular events in the assembly of matrix adhesions at the leading edge of migrating cells. *Journal of cell science* **116**, 4605-13 (2003).

18. Hirata, H., Tatsumi, H. & Sokabe, M. Mechanical forces facilitate actin polymerization at focal adhesions in a zyxin-dependent manner. *Journal of cell science* **121**, 2795-804 (2008).

19. Lele, T.P., Pendse, J.A.Y., Kumar, S., Salanga, M. & Karavitis, J. Mechanical Forces Alter Zyxin Unbinding Kinetics Within Focal Adhesions of Living Cells. **194**, 187-194 (2006).

20. Yoshigi, M., Hoffman, L.M., Jensen, C.C., Yost, H.J. & Beckerle, M.C. Mechanical force mobilizes zyxin from focal adhesions to actin filaments and regulates cytoskeletal reinforcement. *The Journal of cell biology* **171**, 209-15 (2005).

21. Whitesides, G.M., Ostuni, E., Takayama, S., Jiang, X. & Ingber, D.E. Soft lithography in biology and biochemistry. *Annual review of biomedical engineering* **3**, 335-73 (2001).

22. Manuscript, A. NIH Public Access. **59**, 1392-1412 (2009).

23. Alom Ruiz, S. & Chen, C.S. Microcontact printing: A tool to pattern. *Soft Matter* **3**, 168 (2007).

24. Thoumine, O. & Ott, a Time scale dependent viscoelastic and contractile regimes in fibroblasts probed by microplate manipulation. *Journal of cell science* **110 (Pt 1**, 2109-16 (1997).

25. Bausch, a R., Ziemann, F., Boulbitch, a a, Jacobson, K. & Sackmann, E. Local measurements of viscoelastic parameters of adherent cell surfaces by magnetic bead microrheometry. *Biophysical journal* **75**, 2038-49 (1998).

26. Wang, N. & Ingber, D.E. Probing transmembrane mechanical coupling and cytomechanics using magnetic twisting cytometry. *Biochemistry and cell biology = Biochimie et biologie cellulaire* **73**, 327-35 (1995).

27. Radmacher, M., Fritz, M. & Hansma, P.K. Imaging soft samples with the atomic force microscope: gelatin in water and propanol. *Biophysical journal* **69**, 264-70 (1995).

28. Balaban, N.Q. *et al.* Force and focal adhesion assembly: a close relationship studied using elastic micropatterned substrates. *Nature cell biology* **3**, 466-72 (2001).

29. Voldman, J. Electrical forces for microscale cell manipulation. *Annual review of biomedical engineering* **8**, 425-54 (2006).

30. Lo, C.M., Wang, H.B., Dembo, M. & Wang, Y.L. Cell movement is guided by the rigidity of the substrate. *Biophysical journal* **79**, 144-52 (2000).

31. Discher, D.E., Janmey, P. & Wang, Y.-L. Tissue cells feel and respond to the stiffness of their substrate. *Science (New York, N.Y.)* **310**, 1139-43 (2005).

32. Dalby, M.J., Riehle, M.O., Johnstone, H., Affrossman, S. & Curtis, a S.G. In vitro reaction of endothelial cells to polymer demixed nanotopography. *Biomaterials* **23**, 2945-54 (2002).

33. Eyckmans, J., Boudou, T., Yu, X. & Chen, C.S. A hitchhiker's guide to mechanobiology. *Developmental cell* **21**, 35-47 (2011).

34. Grinnell, F. Fibroblast biology in three-dimensional collagen matrices. *Trends in Cell Biology* **13**, 264-269 (2003).

35. Cukierman, E., Pankov, R., Stevens, D.R. & Yamada, K.M. Taking cell-matrix adhesions to the third dimension. *Science (New York, N.Y.)* **294**, 1708-12 (2001).

36. Clark, R.A.F. & Henson, P.M. *The Molecular and Cellular Biology of Wound Repair*. (Plenum: New Yourk, 1988).

37. Gurtner, G.C., Werner, S., Barrandon, Y. & Longaker, M.T. Wound repair and regeneration. *Nature* **453**, 314-21 (2008).

38. Aarabi, S., Longaker, M.T. & Gurtner, G.C. Hypertrophic scar formation following burns and trauma: new approaches to treatment. *PLoS medicine* **4**, e234 (2007).

39. Yarrow, J.C., Perlman, Z.E., Westwood, N.J. & Mitchison, T.J. A high-throughput cell migration assay using scratch wound healing, a comparison of image-based readout methods. *BMC biotechnology* **4**, 21 (2004).

40. Riahi, R., Yang, Y., Zhang, D.D. & Wong, P.K. Advances in wound-healing assays for probing collective cell migration. *Journal of laboratory automation* **17**, 59-65 (2012).

41. Liu, Y. *et al.* Control of cell migration in two and three dimensions using substrate morphology. *Experimental cell research* **315**, 2544-57 (2009).

42. Friedl, P. & Bröcker, E.B. The biology of cell locomotion within three-dimensional extracellular matrix. *Cellular and molecular life sciences : CMLS* **57**, 41-64 (2000).

43. Xie, J. *et al.* Radially Aligned , Electrospun Nanofibers and Tissue Regeneration Applications. **4**, 5027-5036 (2010).

44. Zahedi, P., Rezaeian, I., Ranaei-Siadat, S.-O., Jafari, S.-H. & Supaphol, P. A review on wound dressings with an emphasis on electrospun nanofibrous polymeric bandages. *Polymers for Advanced Technologies* n/a-n/a (2009).doi:10.1002/pat.1625

45. Zahedi, P., Rezaeian, I., Ranaei-Siadat, S.-O., Jafari, S.-H. & Supaphol, P. A review on wound dressings with an emphasis on electrospun nanofibrous polymeric bandages. *Polymers for Advanced Technologies* n/a-n/a (2009).doi:10.1002/pat.1625

46. Rujitanaroj, P.-on, Pimpha, N. & Supaphol, P. Wound-dressing materials with antibacterial activity from electrospun gelatin fiber mats containing silver nanoparticles. *Polymer* **49**, 4723-4732 (2008).

Appendix A:

Derivation of Beam Equation

The modeled beam with a non-uniform distributed load under tension is derived below. The equation is solved by representing the beam deflection as a series of superimposed sine waves. The coefficients of the sine waves for the equation is found by knowing that when an elastic system undergoes a small displacement from its position of equilibrium, the corresponding increase in potential energy of the system is equal to the work done by the external forces during such a displacement. This expression was derived from Timoshenko's Strength of Materials Part II, Advanced theories and Problems.

The deflection of the beam is represented as a series of sine waves:

$$y = \sum_{n=1}^{\infty} a_n \sin\left(\frac{\pi n x}{l}\right)$$

Which is expanded as:

$$y = a_1 \sin\left(\frac{\pi x}{l}\right) + a_2 \sin\left(\frac{2\pi x}{l}\right) + a_3 \sin\left(\frac{3\pi x}{l}\right) + \ldots$$

a_n is solved by equating the elastic strain energy of the beam to the work applied to the beam. The elastic strain energy of a beam is:

$$U = \frac{EI}{2} \int_0^l \left(\frac{d^2y}{dx^2}\right)^2 dx$$

The second derivative of the series of sine waves is:

$$\frac{d^2y}{dx^2} = -\frac{\pi^2}{l^2} \mathrm{a}_1 \sin\left(\frac{\pi x}{l}\right) - \frac{4\pi^2}{l^2} a_2 \sin\left(\frac{2\pi x}{l}\right) - \frac{9\pi^2}{l^2} a_3 \sin\left(\frac{3\pi x}{l}\right) + \cdots$$

Substitute into strain energy equation:

$$\left(\frac{d^2y}{dx^2}\right)^2 = \left(-\frac{\pi^2}{l^2} \mathrm{a}_1 \sin\left(\frac{\pi x}{l}\right) - \frac{4\pi^2}{l^2} a_2 \sin\left(\frac{2\pi x}{l}\right) - \frac{9\pi^2}{l^2} a_3 \sin\left(\frac{3\pi x}{l}\right) + \cdots\right)^2$$

$$U = \frac{EI\pi^4}{2l^4} \int_0^l \left(-\mathrm{a}_1 \sin\left(\frac{\pi x}{l}\right) - 4a_2 \sin\left(\frac{2\pi x}{l}\right) - 9a_3 \sin\left(\frac{3\pi x}{l}\right) + \cdots\right)^2 dx$$

Further Simplification of the expression reveals terms in two forms

$$a_n^2 \frac{n^4\pi^4}{l^4} \sin^2 \frac{n\pi x}{l}$$

And

$$2a_n a_m \frac{n^2 m^2 \pi^4}{l^4} \sin \frac{n\pi x}{l} \sin \frac{m\pi x}{l}$$

These terms can be simplified further with the following integral identities:

$$\int_0^l \sin(\mathrm{mx}) \sin(\mathrm{nx})\, dx = 0 \quad where\ m \neq n$$

$$\int_0^l \sin^2\left(\frac{n\pi x}{l}\right) dx = \frac{l}{2}$$

Integrating and simplifying expression:

$$U = \frac{EI\pi^4}{2l^4} * \frac{l}{2}(a_1^2 + 2^4 a_n^2 + 3^4 a_3^2 + \cdots)$$

Strain energy equation is simplified to:

$$U = \frac{EI\pi^4}{4l^3} \sum_{n=1}^{\infty} a_n^2 n^4$$

The change in strain energy is:

$$dU = \frac{\partial U}{\partial a_n} da_n = \frac{EI\pi^4}{2l^3} n^4 a_n da_n$$

The work done by the distributed load is found first from find the work of a point force, P at position c:

$$da_n \left(\sin\frac{n\pi c}{l}\right) P$$

The work done by a distributed of a force density q between 0 and b is:

$$\int_0^b da_n \left(\sin\frac{n\pi c}{l}\right) q dc$$

$$da_n \frac{lq}{\mathrm{n}\pi}\left(1 - \cos\frac{n\pi b}{l}\right)$$

The work done by a distributed of a force density q between 0 and a is:

$$da_n \frac{lq}{\mathrm{n}\pi}\left(1 - \cos\frac{n\pi a}{l}\right)$$

The work done by the tension is found by finding the difference between the length of the beam at rest and the arc of the deflected beam as a result of tension. The difference is:

$$\lambda = \frac{1}{2}\int_0^l \left(\frac{dy}{dx}\right)^2 dx$$

$$\frac{dy}{dx} = a_1 \frac{\pi}{l} \cos\left(\frac{\pi x}{l}\right) + a_2 \frac{2\pi}{l} \cos\left(\frac{2\pi x}{l}\right) + a_3 \frac{3\pi}{l} \cos\left(\frac{3\pi x}{l}\right) + \ldots$$

$$\lambda = \frac{1}{2} \int_0^l \left(a_1 \frac{\pi}{l} \cos\left(\frac{\pi x}{l}\right) + a_2 \frac{2\pi}{l} \cos\left(\frac{2\pi x}{l}\right) + a_3 \frac{3\pi}{l} \cos\left(\frac{3\pi x}{l}\right) + \ldots\right)^2 dx$$

The square of the expression leaves terms in two forms.

$$\frac{a_n^2 n^2 \pi^2}{l^2} \cos^2 \frac{n\pi x}{l}$$

$$2a_n a_m \frac{nm\pi^2}{l^2} \cos\frac{n\pi x}{l} \cos\frac{m\pi x}{l}$$

These terms can be simplified further with the following integral identities:

$$\int_0^l \cos^2\left(\frac{\pi n x}{l}\right) dx = \frac{l}{2}$$

$$\int_0^l cos\left(\frac{\pi n x}{l}\right) cos\left(\frac{\pi m x}{l}\right) dx = 0 \;\; where \;\; m \neq n$$

Integrating and simplifying expression:

$$\lambda = \frac{1}{2} \sum_{n=1}^{\infty} \frac{a_n^2 n^2 \pi^2}{l^2} * \frac{l}{2}$$

The arc length is simplified as:

$$\lambda = \frac{\pi^2}{4l} \sum_{n=1}^{\infty} a_n^2 n^2$$

The change in arc length is:

$$d\lambda = \frac{\partial \lambda}{\partial a_n} da_n = \frac{\pi^2}{2l} n^2 a_n da_n$$

The work done by tension is the product of the change in arc length and the tension:

$$-S \frac{\pi^2}{2l} n^2 a_n da_n$$

Equate the change in work to strain energy:

$$-S\frac{\pi^2}{2l}n^2a_nda_n + da_n\frac{lq}{n\pi}\left(1-\cos\frac{n\pi b}{l}\right) - da_n\frac{lq}{n\pi}\left(1-\cos\frac{n\pi a}{l}\right) = \frac{EI\pi^4}{2l^3}n^4a_nda_n$$

Simplify expression to find a_n

$$a_n = \frac{2l^4q}{EI\pi^5}\frac{1}{n^3(n^2+\alpha)}\left(\cos\frac{n\pi a}{l} - \cos\frac{n\pi b}{l}\right)$$

Where

$$\alpha = \frac{Sl^2}{EI\pi^2}$$

Finally plug a_n back into the original deflection equation. This gives the final deflection curve

$$y = \frac{2l^4q}{EI\pi^5}\sum_{n=1}^{\infty}\frac{1}{n^3(n^2+\alpha)}\left(\cos\frac{n\pi a}{l} - \cos\frac{n\pi b}{l}\right)\sin\frac{n\pi x}{l}$$

Where

$$\alpha = \frac{Sl^2}{EI\pi^2}$$

Appendix B:

Derivation of Varied Spacing Equation

The derivation of our fiber deposition spacing with a nonzero acceleration is described below:

The translational speed from the perspective of the fiber is a function of the substrate rotational velocity and the stage acceleration:

$$v(t) = \frac{at}{\omega}$$

ω is the rotational velocity, t is the time and a is the acceleration. The position function is found by integrating the velocity:

$$x(t) = \int \frac{at}{\omega} dt$$
$$x(t) = \frac{at^2}{2\omega}$$

The time can be equated to the number of rotations where one fiber is deposited with each rotation

$$t = \frac{n}{\omega}$$

Substituting this term into the position function and representing it as a series

$$x(t) = \sum_{n=1}^{nn} \left(\frac{a(\frac{n}{\omega})^2}{2\omega}\right)$$
$$x(t) = \sum_{n=1}^{nn} \left(\frac{an^2}{2\omega^3}\right)$$

Where nn is the number of fibers deposited.

The fiber separation is than found by finding the difference between the position of a deposited fiber and the previously deposited fiber

$$l = \sum_{n=1}^{nn} \left(\frac{a}{2\omega^3}(n^2 - (n-1)^2)\right)$$

Final equation

$$l = \sum_{n=1}^{nn} \left(\frac{a}{2\omega^3}(2n-1)\right)$$